Cell

Article

Molecular basis of anaphylatoxin binding, activation, and signaling bias at complement receptors

Graphical abstract

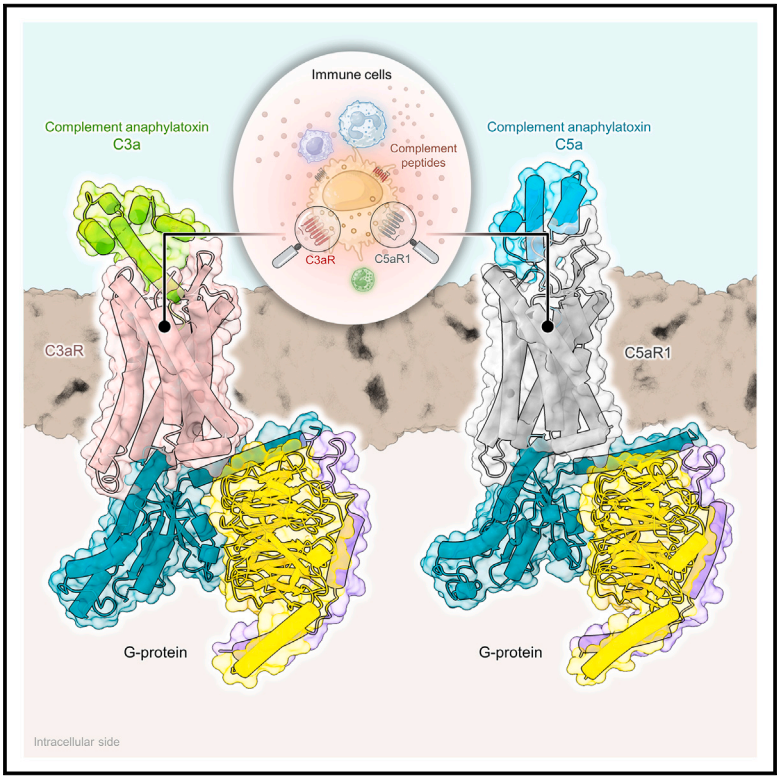

Authors

Manish K. Yadav, Jagannath Maharana, Ravi Yadav, ..., Ramanuj Banerjee, Arun K. Shukla, Cornelius Gati

Correspondence

ramanujb@iitk.ac.in (R.B.), arshukla@iitk.ac.in (A.K.S.), gati@usc.edu (C.G.)

In brief

A series of cryo-EM structures offer insights into how anaphylatoxins C3a and C5a engage complement receptors, illustrating agonist binding modes, pathways of receptor activation, and signaling bias that should facilitate the discovery of ligands and therapeutic candidates targeting these receptors.

Highlights

- Cryo-EM structures of complement receptors C5aR1 and C3aR in complex with G proteins
- Molecular mechanism of ligand binding, selectivity, activation, and signaling bias
- Structural basis of reduced efficacy of $C5a^{des\text{-}Arg}$ through proteolytic cleavage
- Discovery and structural mechanism of a subtype-specific biased agonist of C3aR

Yadav et al., 2023, Cell *186*, 4956–4973
October 26, 2023
https://doi.org/10.1016/j.cell.2023.09.020

CellPress

CellPress
OPEN ACCESS

Cell

Article

Molecular basis of anaphylatoxin binding, activation, and signaling bias at complement receptors

Manish K. Yadav,[1,8] Jagannath Maharana,[1,8] Ravi Yadav,[2,3,8] Shirsha Saha,[1,8] Parishmita Sarma,[1,8] Chahat Soni,[1] Vinay Singh,[1] Sayantan Saha,[1] Manisankar Ganguly,[1] Xaria X. Li,[5] Samanwita Mohapatra,[1] Sudha Mishra,[1] Htet A. Khant,[6] Mohamed Chami,[7] Trent M. Woodruff,[5] Ramanuj Banerjee,[1,*] Arun K. Shukla,[1,9,*] and Cornelius Gati[2,3,4,*]

[1]Department of Biological Sciences and Bioengineering, Indian Institute of Technology, Kanpur 208016, India
[2]Molecular and Computational Biology Section, Department of Biological Sciences, University of Southern California, Los Angeles, CA, USA
[3]The Bridge Institute, Michelson Center for Convergent Biosciences, University of Southern California, Los Angeles, CA, USA
[4]Department of Chemistry, Department of Quantitative and Computational Biology, Alfred E. Mann School of Pharmacy and Pharmaceutical Sciences, University of Southern California, Los Angeles, CA, USA
[5]School of Biomedical Sciences, Faculty of Medicine, The University of Queensland, Brisbane, QLD 4072, Australia
[6]USC Center of Excellence for Nano-Imaging, Viterbi School of Engineering, University of Southern California, Los Angeles, CA, USA
[7]BioEM Lab, Biozentrum, Universität Basel, Basel, Switzerland
[8]These authors contributed equally
[9]Lead contact
*Correspondence: ramanujb@iitk.ac.in (R.B.), arshukla@iitk.ac.in (A.K.S.), gati@usc.edu (C.G.)
https://doi.org/10.1016/j.cell.2023.09.020

SUMMARY

The complement system is a critical part of our innate immune response, and the terminal products of this cascade, anaphylatoxins C3a and C5a, exert their physiological and pathophysiological responses primarily via two GPCRs, C3aR and C5aR1. However, the molecular mechanism of ligand recognition, activation, and signaling bias of these receptors remains mostly elusive. Here, we present nine cryo-EM structures of C3aR and C5aR1 activated by their natural and synthetic agonists, which reveal distinct binding pocket topologies of complement anaphylatoxins and provide key insights into receptor activation and transducer coupling. We also uncover the structural basis of a naturally occurring mechanism to dampen the inflammatory response of C5a via proteolytic cleavage of the terminal arginine and the G-protein signaling bias elicited by a peptide agonist of C3aR identified here. In summary, our study elucidates the innerworkings of the complement anaphylatoxin receptors and should facilitate structure-guided drug discovery to target these receptors in a spectrum of disorders.

INTRODUCTION

One of the key mechanisms through which the immune system combats pathogenic infections is the activation of the complement cascade.[1–4] It is an intricate network of plasma proteins including inflammatory peptides, proteases, and integral membrane receptors that work in a concerted fashion.[1–4] Once activated, it plays a vital role in the efficient elimination of microbial agents through the formation of the membrane attack complex and associated mechanisms.[3,4] Complement activation results in the generation of several peptide fragments by the action of different proteases, and these complement factors subsequently exert their functions through their corresponding receptors and effectors.[1–4] Abnormal activation of the complement system is directly linked with multiple disease conditions, including immunodeficiency, autoimmune disorders such as rheumatoid arthritis, hematological and vascular disease, ocular disease, neurodegenerative and neuropsychiatric disease, renal disease, and inflammatory bowel disease.[5–7] Complement fragments C3a and C5a generated from the proteolytic cleavage of complement C3 and C5, respectively, also known as anaphylatoxins, play a central role in priming and amplifying the immune response by recruiting immune cells, such as leukocytes, and triggering the secretion of pro-inflammatory molecules, such as cytokines.[1–4]

C3a and C5a bind to distinct seven transmembrane receptors (7TMRs), with C3a being selective for C3aR, whereas C5a can bind to two different receptors, namely, C5aR1 and C5aR2[8–11] (Figure 1A). C3aR is a prototypical G-protein-coupled receptor (GPCR), which exhibits primary and secondary coupling to Gi and Gq subtypes of heterotrimeric G proteins and also recruits β-arrestins (βarrs) upon activation[11–14] (Figure 1A). On the other hand, although C5aR1 couples to both Gi and βarrs upon activation by C5a, C5aR2 solely signals via βarrs without any measurable G-protein activation and hence is also referred to as an arrestin-

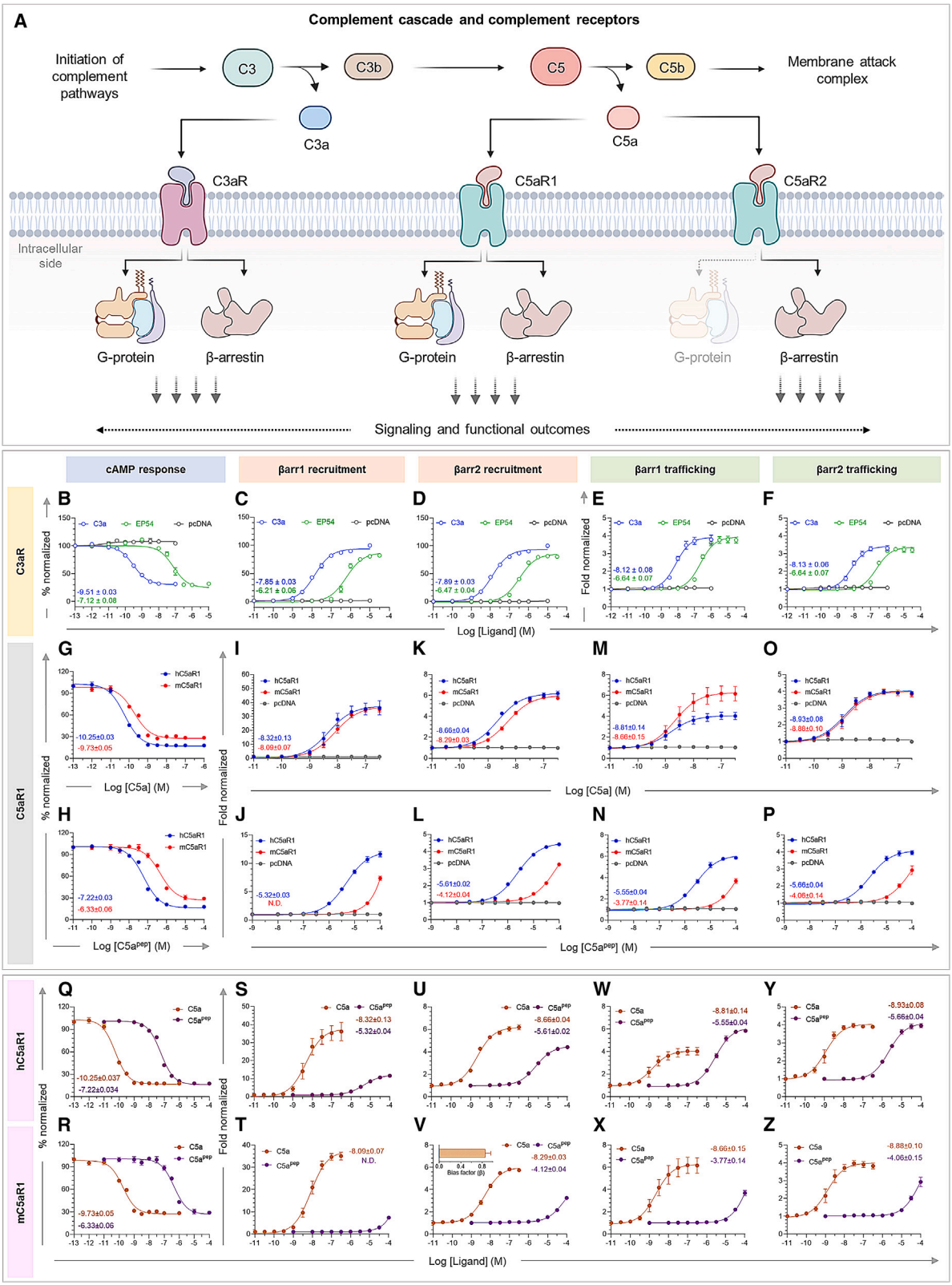

(legend on next page)

coupled receptor (ACR)[15–17] (Figure 1A). C3aR and C5aR1 are expressed in multiple types of immune cells, including mast cells, neutrophils, and monocytes/macrophages, and their aberrant signaling is linked to numerous inflammatory disorders, such as sepsis, vasculitis, pulmonary fibrosis, arthritis, asthma, and lupus,[5,6,18–21] making them important drug targets. Moreover, the interaction of C5a with C5aR1 and ensuing downstream signaling responses have been implicated in the disease severity of COVID-19 patients, including a potential chemoattractant role leading to infiltration of neutrophils and monocytes in the broncho-alveolar lavage fluid (BALF) of patients.[22] In addition, a monoclonal antibody that targets complement C5a and thereby blocks its interaction with C5aR1, has recently been approved for use in hospitalized patients of COVID-19.[23] However, despite its fundamental importance, our current understanding of complement anaphylatoxin recognition by complement receptors remains limited and is based predominantly on biochemical studies.

Human C3a and C5a contain 77 and 74 amino acids, respectively, and exhibit a four-helix bundle architecture.[24,25] Previous studies have suggested a two-site binding mechanism to the corresponding receptors involving the N terminus, the 2nd extracellular loop (ECL2), and the transmembrane core of the receptor.[26–29] Interestingly, peptides derived from and modified based on the carboxyl terminus of both C3a and C5a have been identified as agonists of C3aR and C5aR1, although their binding affinity and potency differ significantly.[16,30–38] For example, EP54 and EP67, two decapeptides derived from the carboxyl terminus of C5a, and several peptides derived from the carboxyl terminus of C3a exhibit full agonism at C3aR in ERK1/2 mitogen-activated protein (MAP) kinase phosphorylation assay.[33] Moreover, a previous study has also reported that EP54 and EP67 can induce cytokine production and, to a lesser extent, enzyme release from neutrophils.[39] Similarly, a hexapeptide designed based on C5a, referred to as C5a^{pep}, behaves as a G-protein-biased agonist for C5aR1.[40] These studies underscore the critical contribution of the carboxyl terminus of C3a and C5a in eliciting transducer coupling and downstream functional responses. Finally, the activity of C3a and C5a is regulated by a physiological mechanism where the terminal arginine residues are cleaved off by the action of carboxypeptidases, and the resulting fragments, referred to as C3a$^{des\text{-}Arg}$ and C5a$^{des\text{-}Arg}$ exhibit a significantly reduced functional responses through the cognate receptors.[41–44] However, the direct structural visualization of agonist binding to C3aR and C5aR1 and ensuing mechanism of receptor activation and transducer coupling still remain elusive. This represents a major knowledge gap in our current understanding of complement receptor activation and signaling that restricts the possibility of structure-guided design of ligands and therapeutics targeting these receptors.

In this manuscript, we present nine cryoelectron microscopy (cryo-EM) structures of agonist-bound C3aR and C5aR1 in complex with heterotrimeric G proteins, which elucidate intricate molecular details of complement recognition, receptor activation, and downstream signaling. In particular, these structures uncover previously unanticipated distinct binding modes for C3a and C5a on their respective receptors while maintaining a converged positioning of their carboxyl terminus in the binding pocket. The structural insights help rationalize the subtype selectivity of C3a and C5a, a large body of data on agonism and cross-reactivity of C3a/C5a-derived peptides, and allow us to identify a subtype-selective G-protein-biased agonist at C3aR. Together with biochemical and pharmacological data, the structural snapshots presented here unravel the molecular mechanism driving signaling bias in the complement receptor system and the natural mechanism to dampen the inflammatory responses of complement anaphylatoxins through the removal of the terminal arginine residue. Collectively, this study offers a previously lacking platform to facilitate structure-guided drug discovery at the complement receptors with enhanced subtype selectivity and biased agonism.

Figure 1. Activation of complement receptors and downstream functional outcomes

(A) Triggering of the various complement pathways leads to the generation of complement peptides and subsequent activation of cognate complement receptors. An overview of the activation of C3aR, C5aR1, and C5aR2 and their signaling has been illustrated.

(B) To study Gαi activation, forskolin-elevated decrease in cAMP level is measured using GloSensor assay downstream of C3aR in response to indicated ligands (mean ± SEM; n = 4; normalized with starting value for each ligand as 100%).

(C and D) βarr1/2 recruitment to C3aR in response to indicated ligands as measured by NanoBiT assay (receptor-SmBiT + LgBiT-βarr1/2), respectively (mean ± SEM; n = 4; normalized with the luminescence signal at maximal ligand dose of C3a as 100%).

(E and F) βarr1/2 trafficking to the endosomes downstream of C3aR in response to indicated ligands as measured by NanoBiT assay (receptor + SmBiT-βarr1/2 + LgBiT-FYVE) (mean ± SEM; n = 4; normalized with the luminescence signal at minimal ligand dose of each condition as 1).

(G and H) C5a (top) and C5a^{pep} (bottom) driven Gαi-mediated second messenger response as measured by agonist-dependent decrease in forskolin-induced cytosolic cAMP levels downstream to C5aR1. Respective logEC50 values are mentioned in the inset. Data (mean ± SEM) represent four independent experiments, normalized with respect to the highest signal (measured as 100%) for each receptor.

(I–P) C5a/C5a^{pep} induced βarr1/2 recruitment and trafficking as measured by NanoBiT assay. Respective logEC50 values are mentioned in the inset. Data (mean ± SEM) represent four independent experiments, fold normalized with respect to luminescence observed at the lowest dose (measured as 1) for each receptor.

(Q and R) Comparison of C5a/C5a^{pep}-mediated cAMP response downstream of human (top) and mouse (bottom) C5aR1 reveals reduced potency of C5a^{pep} as compared with C5a. Respective logEC50 values are mentioned in the inset. Data (mean ± SEM) represent four independent experiments, normalized with respect to the highest signal (measured as 100%) in response to each ligand.

(S–Z) Measurement of βarr1/2 recruitment and trafficking to human (top) and mouse (bottom) C5aR1 upon stimulation with C5a and C5a^{pep}. Respective logEC50 values are mentioned in the inset. Data (mean ± SEM) represent four independent experiments, fold normalized with respect to luminescence observed at the lowest dose (measured as 1) for each ligand. Bias factor (β value) determined by taking C5a as reference elucidates the G-protein-biased nature of C5a^{pep} that has been provided in insets.

Plots explaining the functional bias (Q–Z) of C5a^{pep} are from the data shown in (G)–(P) and presented separately to highlight the effects compared with C5a in both human and mouse C5aR1.

See also Figure S1.

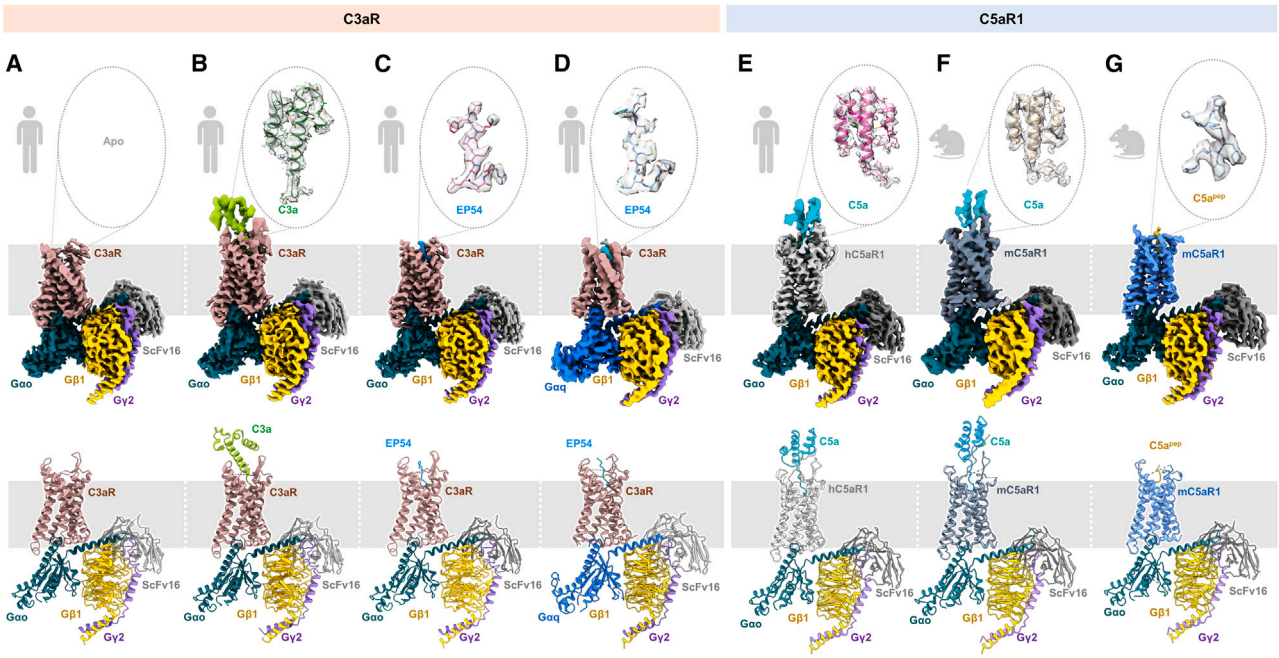

Figure 2. Structures of complement receptor signaling complexes

(A–G) Cryo-EM density maps (top) and corresponding models (bottom) of Apo-C3aR-Go (Glacios), C3a-C3aR-Go, EP54-C3aR-Go, EP54-C3aR-Gq, C5a-hC5aR1-Go, C5a-mC5aR1-Go, and C5a^{pep}-mC5aR1-Go. Cryo-EM density maps of respective ligands have been shown in gray dotted circles (top corner). (Rosy brown, C3aR; green, C3a; pale blue, EP54; light gray, hC5aR1; slate gray and blue, mC5aR1; cyan, C5a; yellow, C5a^{pep}; teal, Gαo; deep blue, Gαq; gold, Gβ1; purple, Gγ2; dark gray, ScFv16.)

See also Table S1 and Methods S1.

RESULTS

Ligand pharmacology at the complement receptors

In order to study agonist binding and activation of C3aR and C5aR1, we focused our efforts on both natural and synthetic agonists of these two receptors. For C3aR, we selected C3a and a decameric peptide agonist EP54. We first measured the pharmacological profile of EP54 with C3a as a reference in G-protein and βarr assays (Figures 1B–1F and S1A–S1C). We observed that EP54 acts as a full agonist for Gαi coupling, as measured using cyclic AMP (cAMP) response in a GloSensor assay, and βarr1/2 recruitment and endosomal trafficking as measured using NanoBiT-based assays, albeit with lower potency (Figures 1B–1F). These findings make EP54 a suitable candidate, together with C3a, to decipher the structural determinants of C3a recognition and agonism at C3aR. In order to further our understanding of complement receptor activation, we next turned our attention to the complement C5a receptor, C5aR1. Previous studies have suggested that selected ligands exhibit species-specific differences in their pharmacology at C5aR1.[20] Therefore, we first compared the pharmacology of human C5a and C5a^{pep}, a synthetic peptide designed based on the carboxyl-terminal sequence of C5a, on the human and mouse C5aR1, referred to as hC5aR1 and mC5aR1, respectively, in G-protein and βarr assays. We observed that both C5a and C5a^{pep} behave as full agonists on mC5aR1 with slightly lower potency compared with hC5aR1 in terms of G-protein-mediated cAMP response (Figures 1G and 1H). On the other hand, although C5a exhibits full agonism for βarr recruitment and endosomal trafficking on mC5aR1 (Figures 1I, 1K, 1M, and 1O), C5a^{pep} displays partial agonism at mC5aR1 compared with hC5aR1 in these assays (Figures 1J, 1L, 1N, and 1P). Moreover, C5a^{pep} acts as G-protein-biased agonist at both hC5aR1 and mC5aR1 (Figures 1Q–1Z). The mC5aR1 and hC5aR1 were expressed at comparable levels in these assays (Figures S1D–S1M). These findings suggest that structural visualization of agonist-bound human and mouse C5aR1 may yield interesting insights into species-specific agonist pharmacology. We also note that in some assays, C5a^{pep} dose-response curves do not reach complete saturation phase due to limitations associated with its relatively lower affinity and poor solubility at higher concentrations, and therefore, we have not calculated bias factor for the corresponding datasets.

Structure determination of agonist-C3aR/C5aR1-G-protein complexes

Taking the lead from the agonist pharmacology data presented in Figure 1, we determined seven different cryo-EM structures of G-protein-bound C3aR and C5aR1 occupied with natural and synthetic agonists (Figures 2A–2G). First, we reconstituted C3a-C3aR-Gαoβ1γ2 complex stabilized by ScFv16[30] (Methods S1) and determined the structure at ~3.2 Å (Methods S1). However, we did not observe any discernible density for C3a in the complex (Figure 2A). We, therefore, refer to this as

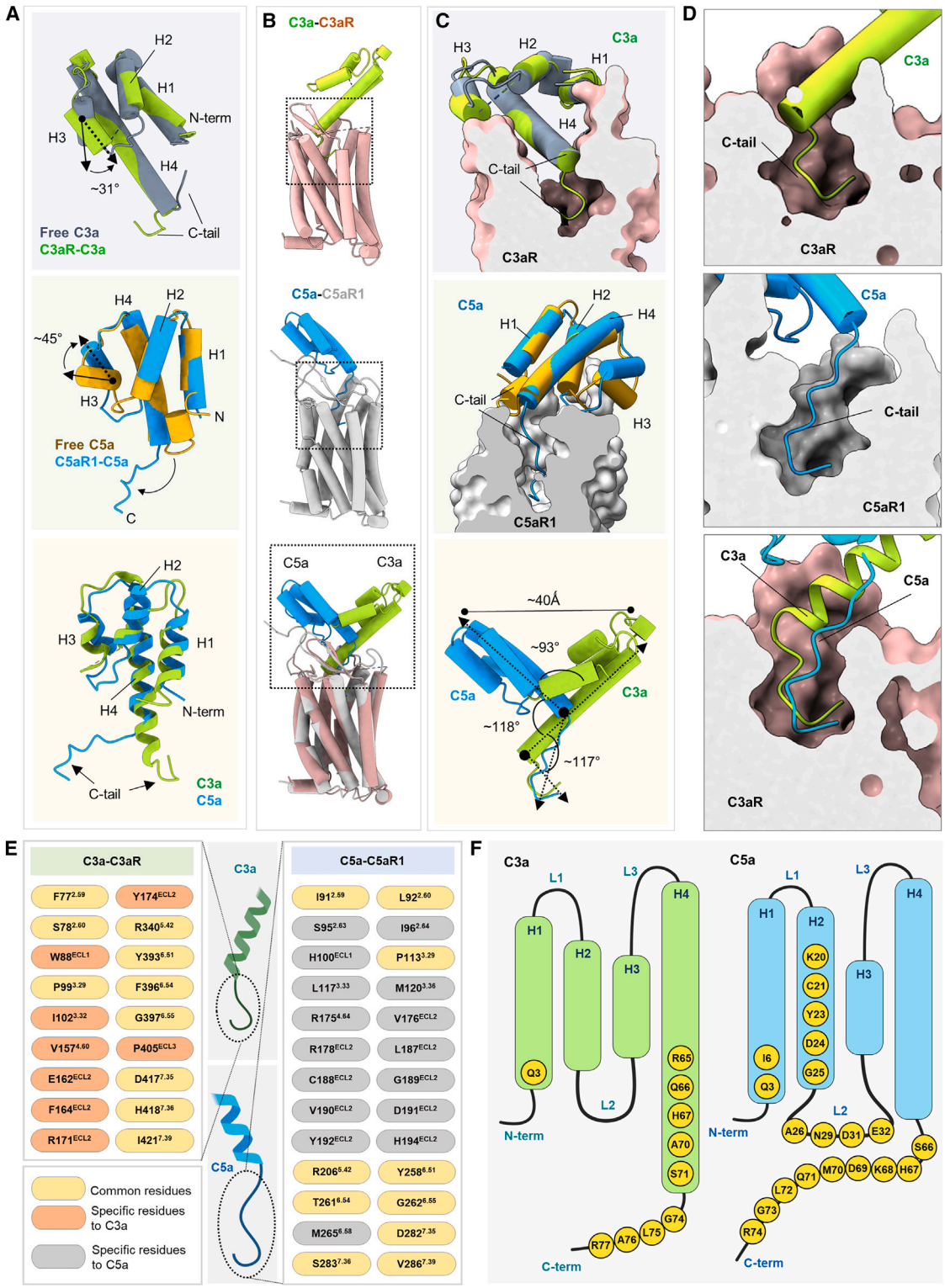

Figure 3. Complement peptide binding to complement receptors

(A) Structure of C3a (top) and C5a (middle), showing four-helix bundle with a short C-terminal tail. Free C3a (PDB: 4HW5) and free C5a (PDB: 1KJS) have been superimposed with C3a and C5a, respectively. Structural alignment of C3a and C5a in receptor-bound forms (bottom).

(B) Side view of C3aR (top), C5aR1 (middle), and both (bottom) bound to their endogenous ligands.

(C) The C termini of the ligands change their conformation upon binding to their corresponding receptors compared with the basal states.

(legend continued on next page)

apo-C3aR-Go complex in subsequent discussion. Considering the potential dissociation of C3a during purification as a plausible reason for the empty ligand-binding pocket, we supplemented the reconstituted C3a-C3aR-Gαoβ1γ2 complex with additional C3a immediately before freezing the samples for cryo-EM. This strategy allowed us to obtain a C3a-C3aR-Gαoβ1γ2 complex structure at 3.2 Å with a clear C3a density (Figure 2B; Methods S1). Next, we also reconstituted EP54-C3aR-Gαoβ1γ2 and EP54-C3aR-Gαqβ1γ2 complexes (Methods S1) and determined their structures at 2.9 and 3.6 Å, respectively (Methods S1), and we observed clear densities for EP54 in these complexes (Figures 2C and 2D). Finally, we reconstituted C5a-hC5aR1-Gαoβ1γ2, C5a-mC5aR1-Gαoβ1γ2, and $C5a^{pep}$-mC5aR1-Gαoβ1γ2 complexes and determined their structures at 3.3, 3.9, and 3.4 Å, respectively (Figures 2E–2G; Methods S1). Despite the modest resolution of the mC5aR1 complexes, our generated cryo-EM maps allowed unambiguous modeling of the secondary structures of all components, including C5a and $C5a^{pep}$ (Figures 2F and 2G). The overall data collection and refinement statistics, the density maps of the key segments in the complexes, including the ligands, and the description of the residues that are resolved in these structures are presented in Tables S1 and S2 and Methods S1.

Recognition of complement anaphylatoxins by C3aR and C5aR1

C3a and C5a share about 35% sequence identity, and they both adopt a four-helix bundle architecture stabilized by multiple disulfide bridges and a terminal arginine located at the end of helix 4 (H4)[24,25] (Arg^{77} in C3a and Arg^{74} in C5a) (Figure 3A). Site-directed mutagenesis studies, coupled with ligand binding and second messenger assays, have proposed a two-site model for C3a-C3aR and C5a-C5aR1 interaction, with the first site involving the ECL2 of the receptor, whereas the second site engages multiple residues from the extracellular side of the transmembrane domain (TMD).[26,27] In addition, the N terminus of C5aR1 has also been proposed to be involved in C5a binding.[9] It is noteworthy that, although ECL2 of C3aR is extraordinarily long, with more than 150 amino acids, functional studies have demonstrated that a large part of it is dispensable for the binding of C3a, as measured by calcium response assays.[27] In the structures determined here, the stretch from $Lys175^{ECL2}$ to $Pro330^{5.32}$ is not resolved, likely due to inherent flexibility in this region. We observe that both C3a and C5a retain their helical fold upon binding to their respective receptors (Figure 3A), although there are some structural changes compared with their basal states, which are more pronounced in C5a than in C3a (Figure 3A). For example, H3 in C3a and C5a tilts by about 30° and 45°, respectively, upon binding to their corresponding receptors (Figure 3A). Moreover, the distal carboxyl terminus in C3a undergoes a significant rotation upon binding to C3aR (Figure 3A, upper), whereas that in C5a transitions from a short α-helical turn in the basal state to an extended conformation upon binding to C5aR1 (Figure 3A, middle). Surprisingly, there is a dramatic difference in the overall positioning of C3a on C3aR and C5a on C5aR1 (Figures 3B and 3C). The globular domains of C3a and C5a are tilted at an angle of about 120° with respect to their carboxyl terminus (Figure 3C, lower). Moreover, the globular domains of C3a and C5a are oriented in opposite directions on the extracellular side of the receptor at an angle of about 90° (Figure 3C, lower). Notably, however, the carboxyl terminus of both C3a and C5a adopt a hook-like conformation (Figure 3D) and position themselves in an analogous binding pocket on the respective receptors with a buried surface area of 1,720 and 1,252 $Å^2$, respectively (Figure 3D, lower). It is worth noting that the residues from Arg^{65} to Arg^{77} in C3a form extensive interactions with ECL1–ECL3 and TM2–7 in C3aR (Figures 3E and 3F; Table S2). The only other residue from C3a that interacts with C3aR is Gln^{3}, which engages with Asp167 and Thr166 in ECL2 through polar interactions (Figure S1S). On the contrary, we observed a significantly broader interface between C5a and C5aR1, which not only includes Ser^{66} to Arg^{74} at the distal carboxyl terminus but also multiple residues from the loop between H2 and H3, H2, and H1 (Figures 3E, 3F, and S1T). On the receptor side, C3a and C5a engage several analogous residues from TM2–3 and TM5–7, although they also display several specific interactions with their cognate receptors (Figure 3E; Table S2). Importantly, although we observe a clear density for the N terminus of C5aR1 and its interaction with C5a in the C5a-C5aR1 structures, the N terminus of C3aR is not resolved in any of the structures. Although the absence of clearly resolved density for the N terminus of C3aR may indicate its inherent flexibility and a lesser contribution in agonist binding as indicated earlier,[27] future studies are required to probe this further. Taken together, the potential differential involvement of the N terminus and distinct orientation of C3a and C5a provide the structural basis of subtype selectivity between these two receptors. On the other hand, an overall analogous binding pocket and positioning of distal carboxyl terminus of C3a and C5a may help rationalize the cross-reactivity of peptide agonists described earlier.[28] The structure of C5a-bound mouse C5aR1 exhibits an overall similar binding pose of C5a as the human C5aR1, including the extended helical conformation of its distal carboxyl terminus (Figure S1U), extensive interactions with the receptor, including the N terminus and ECL2, and a critical involvement of its terminal Arg^{74} (Table S2).

As mentioned earlier, we serendipitously determined the structure of ligand-free C3aR-Gαoβ1γ2 complex, which exhibits an empty ligand-binding pocket (Figure 2A). Structural comparison between ligand-free and agonist-bound C3aR structures revealed an overall similar conformation of the ligand-binding

(D) The C-terminal tails of C3a (top) and C5a (middle) adopt a hook-like conformation upon entering deep into the orthosteric pocket of respective receptors. C3aR and C5aR1 have been shown in surface slice, and C3a/C5a as cartoon representation.
(E) The distal C-terminal portions of C3a/C5a make extensive contacts with C3aR/C5aR1. Residue at the interface between the H4 and C termini of C3a/C5a and C3aR/C5aR1 is depicted.
(F) C3a and C5a are shown in topology diagrams. Residues making contact with receptors are highlighted in yellow circles.
See also Figures S1 and S2 and Table S2.

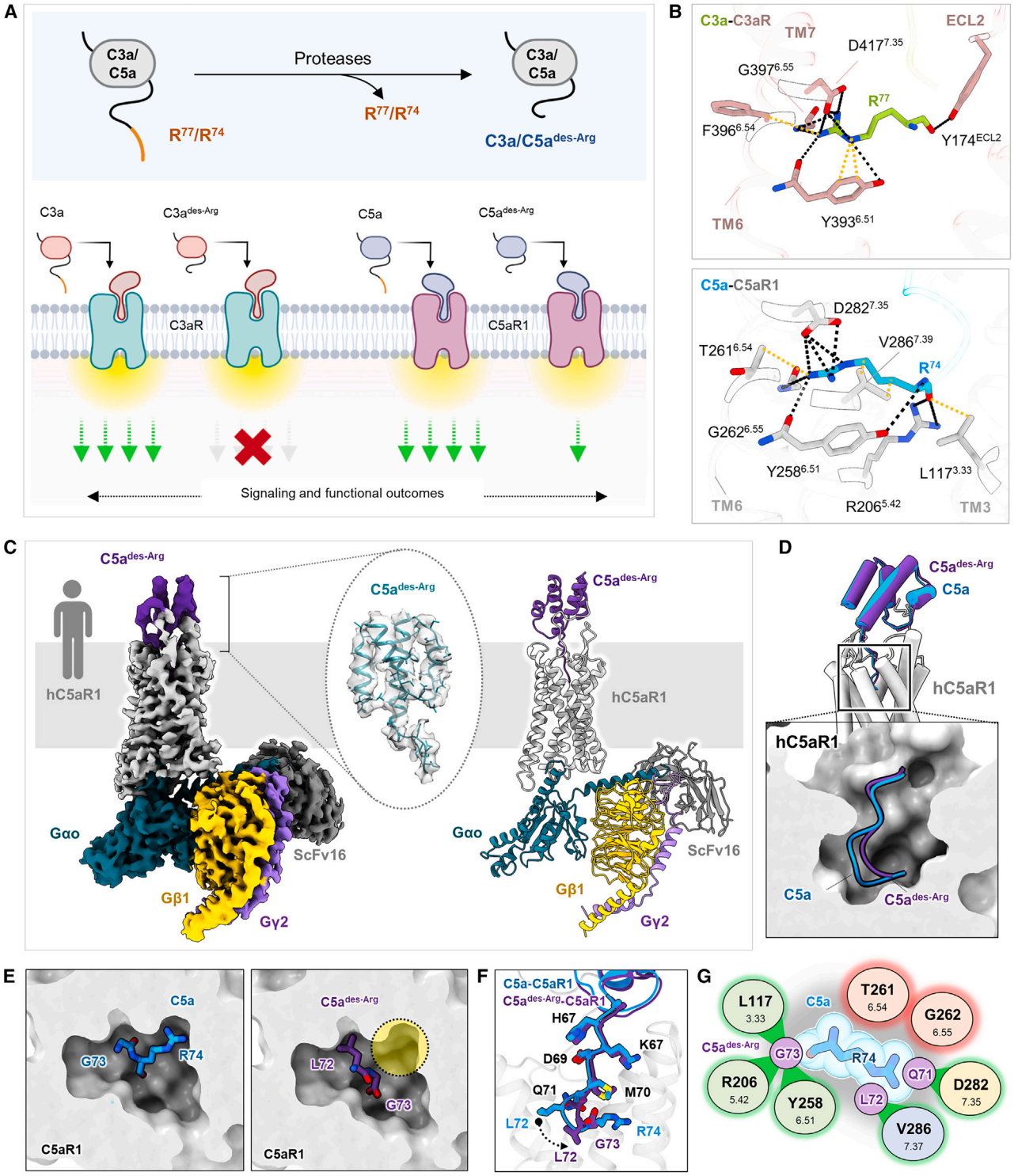

Figure 4. Structural determinants of reduced functional efficacy of C3a$^{des-Arg}$ and C5a$^{des-Arg}$

(A) Proteolytic cleavage of the C-terminal Arg^{77} from C3a and Arg^{74} from C5a results in C3a$^{des-Arg}$ and C5a$^{des-Arg}$, respectively (top). C3a$^{des-Arg}$ is reported to elicit almost no functional outcomes upon binding to C3aR, whereas C5a$^{des-Arg}$ retains minimal potency in driving downstream signaling via C5aR1 (bottom).

(B) Interactions of Arg^{77} in C3a (top) and Arg^{74} in C5a with the residues of C3aR and C5aR1 have been illustrated.

(C) Cryo-EM density map (left) and corresponding model (right) of C5a$^{des-Arg}$-hC5aR1-Go. Cryo-EM density map of C5a$^{des-Arg}$ has been shown in gray dotted circles.

(legend continued on next page)

pocket in C3aR (Figures S2A–S2D), although with a few notable differences (Figures S2E and S2F). For example, Arg340$^{5.42}$ of C3aR, which engages with Arg^{77} of C3a, displays a linear inward shift of about 5 Å, possibly due to a lack of constraints imposed by ligand binding (Figure S2E). Similarly, Arg161$^{4.64}$ in TM4 of C3aR, which engages with Leu^{8} in EP54, exhibits a rotation of about 150° in apo-C3aR, which allows it to interact with the main chain of Lys96$^{3.26}$ in TM3 (Figure S2F).

Structural mechanism of reduced efficacy by C3a$^{des\text{-}Arg}$ and C5a$^{des\text{-}Arg}$

C3a and C5a are potent anaphylatoxins with strong inflammatory response, and there exists a natural mechanism to dampen their excessive activity in physiological context. The terminal arginine residues (Arg^{77} in C3a and Arg^{74} in C5a) are cleaved off by carboxypeptidases, resulting in C3a$^{des\text{-}Arg}$ and C5a$^{des\text{-}Arg}$ (Figure 4A).[6] Although C5a$^{des\text{-}Arg}$ retains about one-tenth of the activity compared with C5a, C3a$^{des\text{-}Arg}$ appears to completely lose the pro-inflammatory activity (Figure 4A).[8,41–43] However, a molecular basis to explain this mechanism operating *in vivo* has remained elusive, and our structural snapshots now provide a potential rationale for this. It is particularly striking that Arg^{77} in C3a and Arg^{74} in C5a form multiple polar interactions and non-bonded contacts with the residues in TMDs and ECL2 of C3aR and C5aR1, respectively (Figure 4B). This is also supported by site-directed mutagenesis studies where Arg^{340}Ala and Asp^{417}Ala mutations in C3aR, which are critical interaction partners of Arg^{77} in C3a, diminish agonist binding and receptor activation.[26] In order to directly elucidate the molecular mechanism of dramatically altered functional efficacy of C5a$^{des\text{-}Arg}$, we reconstituted and determined the structure of C5a$^{des\text{-}Arg}$-C5aR1-Go complex (Figures 4C, S2G, S4D, and S5; Tables S1 and S2). We observed that the binding pose of C5a$^{des\text{-}Arg}$ on C5aR1 superimposes well with C5a, and its carboxy terminus adopts a similar hook-like conformation in the orthosteric binding pocket on the receptor (Figure 4D). Strikingly, however, a minor sub-pocket occupied by Arg^{74} is empty in case of C5a$^{des\text{-}Arg}$ (Figure 4E), and three terminal residues, namely Gln^{71}, Leu^{72}, and Gly^{73}, display spatial repositioning compared to C5a (Figure 4F). Although this repositioning in C5a$^{des\text{-}Arg}$ compensates for some of the interactions made by C5a, two critical interactions with Thr261$^{6.54}$ and Gly262$^{6.55}$ in TM6 are absent (Figure 4G). Arg^{74} in C5a is involved in most extensive interactions in the binding pocket, and therefore, C5a$^{des\text{-}Arg}$ is able to maintain at least some level of transducer coupling through compensating interactions but not at the same level as C5a due to lack of engagement of the Arg^{74} sub-pocket and key missing interactions with TM6 residues.

Structural basis of agonism exhibited by carboxyl-terminal C3a/C5a peptides

In order to gain insights into the mechanism of receptor agonism exhibited by C3a and C5a carboxyl terminus peptides, we analyzed the EP54-C3aR-Go and C5a^{pep}-mC5aR1-Go structures. We observed that similar to the carboxyl terminus of C3a and C5a, EP54 and C5a^{pep} also adopt hook-like conformations and position themselves in a similar binding pocket on the corresponding receptors (Figures 5A and 5B). Specifically, the binding pocket of EP54 and C5a^{pep} on C3aR and C5aR1 are primarily similar to that of C3a and C5a, with buried surface area of 1,640 and 1,140 Å^2, respectively, and a major involvement of TM2–3, TM5–7, ECL2, and ECL3 (Figures 4C and 4D; Table S2). Moreover, the terminal Arg^{10} of EP54 and d-Arg^{6} in C5a^{pep} are positioned in a similar fashion as Arg^{77} and Arg^{74} in C3a and C5a and make similar contacts with key residues in the binding pocket (Figures S1V–S1W). These observations provide a structural rationale for the ability of peptides derived from the carboxyl terminus of C3a and C5a to act as potent receptor agonists and, therefore, also identify ligand-receptor interactions that are critical and sufficient for driving downstream responses. It is also important to note that there are a few interactions that are specific to either EP54 vs. C3a, and C5a^{pep} vs. C5a (Figures 5C and 5D), and it is tempting to speculate that they are responsible for driving lower potency of EP54 and C5a^{pep} compared with C3a and C5a as observed in functional assays (Figures 1B–1P). Finally, the overall binding pose and interactions of EP54 in the C3aR-Gq complex were similar to that in the C3aR-Go complex (Figures S3A–S3E).

Structure-guided reversal of species-specific pharmacology at C5aR1

As presented earlier, we observed only a small difference between human and mouse C5aR1 for C5a-induced G-protein coupling, whereas βarr interaction and trafficking were identical. On the other hand, βarr recruitment and trafficking were dramatically different between the human and mouse receptors upon C5a^{pep} stimulation. Structural superimposition of the human and mouse C5aR1 with respect to C5a- and C5a^{pep}-interacting residues provides the potential structural basis for this observation (Figure 5E). Although the binding poses of C5a^{pep}/C5a on mC5aR1 and C5a on hC5aR1 are similar and the carboxyl terminus hooks occupy similar orientations within the orthosteric pocket, minor rearrangements can be seen in the core helices of C5a (Figure 5F). These helical rearrangements result in significant variation in the docking poses of the N terminus onto C5a in both mouse and human C5aR1 (Figure 5F). Although there are some differences in C5a-interacting residues between the human and mouse receptors, they appear to be minor (Figure 5G). On the other hand, the differences are more

(D) Structural superimposition of C5a- and C5a$^{des\text{-}Arg}$-bound C5aR1 highlighting a similar binding pose. The hook-like C termini of both the ligands are shown within the ligand-binding pocket.
(E) The sub-pocket in C5aR1 occupied by the guanidinium side chain of Arg^{74} is empty in case of C5a$^{des\text{-}Arg}$.
(F) Conformational switching of Leu^{72} and Gly^{73} located toward the distal end of C5a$^{des\text{-}Arg}$ is shown.
(G) Residue contacts by Arg^{74} of C5a in C5aR1 have been shown in circles. Interactions of Gln^{71}, Leu^{72}, and Gly^{73} compensate for the missing terminal Arg in C5a$^{des\text{-}Arg}$ are shown as green circles. Residues highlighted in red do not make any interactions in C5a$^{des\text{-}Arg}$-bound C5aR1 structure.
See also Figures S1 and S7, Table S2, and Methods S1.

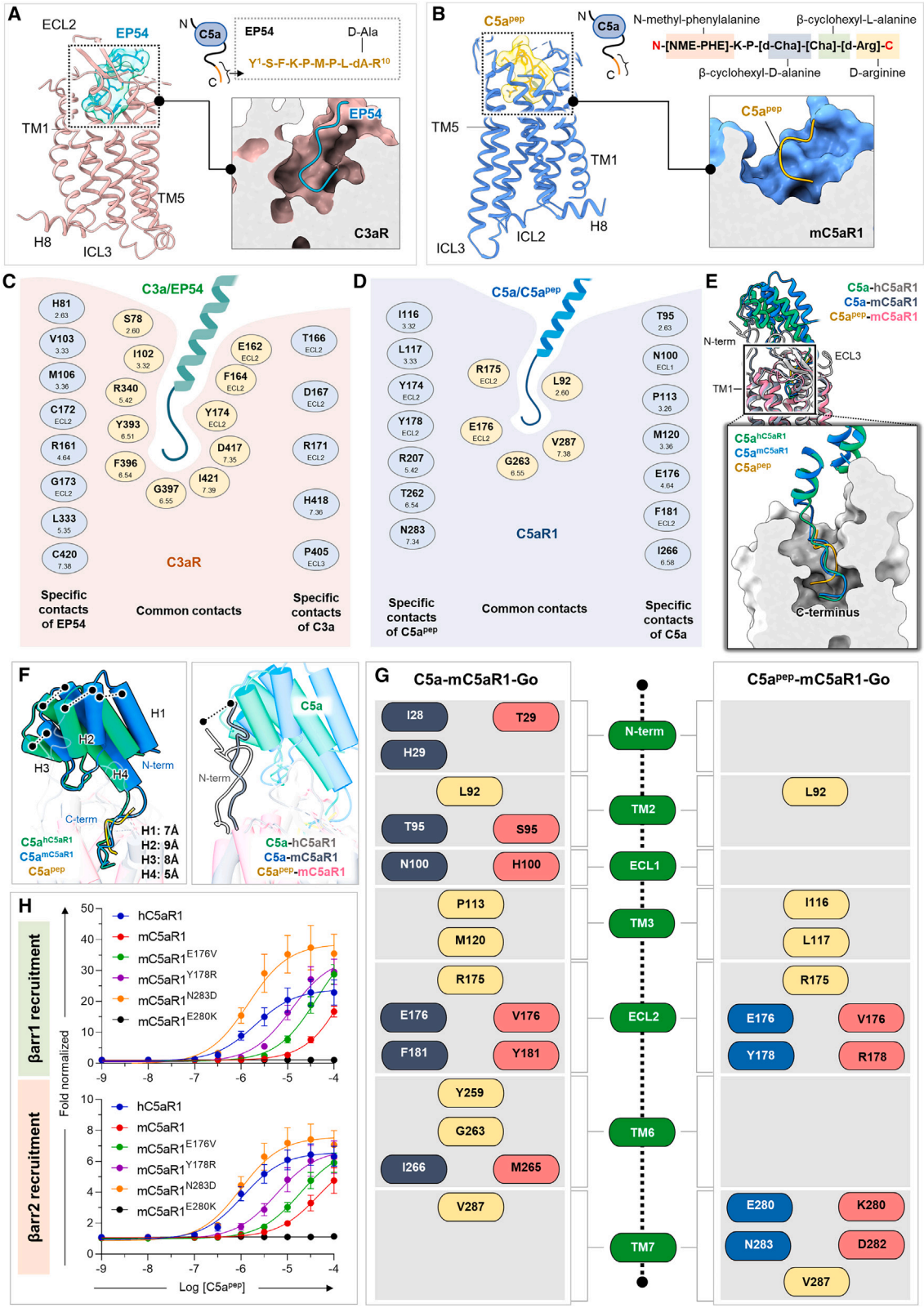

(legend on next page)

pronounced in case of C5a^{pep} interacting residues (Figure 5G). For example, Glu176^{ECL2}, Tyr178^{ECL2}, Glu280$^{7.31}$, and Asn283$^{7.34}$ in mouse C5aR1 are substituted with Val176^{ECL2}, Arg178^{ECL2}, Lys280$^{7.31}$, and Asp282$^{7.34}$, respectively, in human C5aR1 (Figure 5G). In the structure of C5a^{pep}-mC5aR1, Tyr178^{ECL2} interacts with d-Cha^{4} in the ligand, and substitution of Tyr with Arg would reverse the polarity in these positions. Likewise, substitution of Glu280$^{7.31}$ and Asn283$^{7.34}$ in mouse C5aR1 with Lys and Asp, respectively, would alter the individual polarity patterns and possibly allow differential interactions in these sites. These alterations between the amino acid sequence of mouse and human C5aR1 may account for the difference observed in βarr recruitment and trafficking between the human and mouse receptors upon C5a^{pep} stimulation (Figures 1J–1P). In fact, mutating these residues in mouse C5aR1 to the corresponding human C5aR1 residues enhances the potency and efficacy of C5a^{pep} in βarr1/2 recruitment, which supports the structural interpretation outlined above (Figures 5H, S1N, and S1O). Although additional studies are required to correlate the structural observations with functional differences, it provides a plausible structural explanation for species-specific differences in the pharmacology of C5aR1.

Agonist-induced activation and G-protein coupling of the complement receptors

The structural snapshots determined in this study provide comprehensive insights into agonist-induced complement receptor activation. Considering that the only inactive-state structure of the complement receptor family is the antagonist-bound C5aR1 structure,[45,46] we used the same to identify activation-dependent structural features in both C3aR and C5aR1 (Figures 6A, 6B, and S4A). Superimposition of the C3aR structures determined here with antagonist-bound C5aR1 reveals significant conformational changes on the intracellular side of the receptor, including an outward movement of TM6 by approximately 9 Å and an inward shift of TM7 by about 11 Å (Figure 6A). Similar to C3aR, C5aR1 also exhibits the major hallmarks of GPCR activation, including a large outward movement of TM6 by approximately 8 Å, and an inward movement of TM7 by about 10 Å (Figure 6B). Interestingly, in the inactive-state structure of C5aR1, H8 exhibits an inverted orientation and is sandwiched between TM1 and TM7, whereas in both C3aR and C5aR1, H8 undergoes a dramatic movement of nearly 180° compared with the inactive C5aR1 structure, which potentially facilitates the opening of the transducer-coupling interface on the receptor (Figures 6A and 6B). However, we note that the dramatic reorientation of H8 observed here compared with the crystal structure in the inactive state requires further investigation in future studies, preferably in cellular context to establish its functional significance. In addition, the conserved microswitches in C3aR and C5aR1, including DRY, NPxxY, CWxP, and PIF motifs, exhibit significant structural rearrangements upon activation, as outlined in Figures 6C and 6D. We also note that the overall movement of TM6 and TM7, the rotation of H8, and the activation-dependent conformational changes in the microswitches are conserved in all the structures (Figures S4B–S4H and S5). Taken together, these interactions promote the opening of a cavity toward the cytoplasmic face of the receptor, capable of accommodating G protein and the core interaction with βarrs (Figure S4I).

The overall interaction interface between the complement receptors and Gαo is very similar in all structures (Figures 6E, 6F, and S6). For example, the carboxyl terminus of the α5 helix in Gαo adopts a loop conformation and inserts into the cytoplasmic core of the receptor with an approximate buried surface area of 2,200 and 1,800 Å^2 for C3aR and C5aR1, respectively. The key interaction interfaces are composed of TM2, TM3, TM6, TM7, ICL2, and ICL3 in the receptors and α5 helix, αN helix, and αN-β1 loop of the Gαo subunit (Figures 6G, 6H, and S6). Moreover, the overall engagement and interaction interface of C3aR with Gq is similar to that observed for C3aR-Go complex, although there are some differences, as well (Figures S3E and S6). A comprehensive list of all the receptor-G-protein interfaces is included in Table S2, and the EM densities of the critical residue-level interactions are presented in Figure S7.

Discovery of a G-protein-biased agonist at C3aR

Based on the structural insights wherein the terminal carboxyl segments of the C3a and C5a appear to be most critical for receptor binding and activation, we tested a set of peptide ligands including C3a and C5a on C3aR and C5aR1 in G-protein-coupling and βarr-recruitment assays (Figures 7A and S1P–S1R). Interestingly, although C3a did not exhibit any measurable

Figure 5. Binding poses of C3a- and C5a-derived peptides on C3aR and C5aR1 and species-specific insights into ligand binding of C5aR1

(A) Sequence of EP54 derived from the C terminus of C5a (top right). Side view of EP54 (transparent surface) binding to C3aR (ribbon) (left). EP54 docks into C3aR and forms a hook-like structure (bottom right).

(B) Sequence of C5a^{pep} derived from the C terminus of C5a (top right). Side view of C5a^{pep} (transparent surface) binding to C5aR1 (ribbon) (left). C5a^{pep} docks into C5aR1 and forms a hook-like structure (bottom right).

(C and D) Comparative analysis of common and specific interactions of C3a/EP54 with C3aR and C5a/C5a^{pep} with C5aR1.

(E) Superimposition of agonist-C5aR1 structures. C5a and C5a^{pep} in the ligand-binding pocket are shown. (hC5aR1 in surface slice and ligands in cartoon representation.)

(F) Helical shifts in the core domain of C5a upon binding to mouse and human C5aR1 are shown (left). Conformational changes in the N termini of mouse and human C5aR1 upon interaction with C5a (right).

(G) Schematic representation of residue contacts between C5a and C5a^{pep} with mC5aR1. Residues present at the orthosteric pocket of ligand binding are depicted. Residues from C5a-hC5aR1 structure shown in red boxes, C5a-mC5aR1 structure in dark gray, C5a^{pep}-mC5aR1 in blue, and common residue contacts at the interface have been shown in yellow boxes. Different regions from the receptors have been highlighted in green boxes.

(H) Measuring βarr1/2 recruitment in response to C5a^{pep} downstream to a series of mC5aR1 mutants mimicking the corresponding hC5aR1 residues show dramatic increase in both potency and efficacy of βarr1/2 recruitment compared with the wild-type mouse receptor. Data (mean ± SEM) represent six independent experiments, fold normalized with respect to luminescence observed at the lowest dose (measured as 1) for each receptor.

See also Figures S1 and S3 and Table S2.

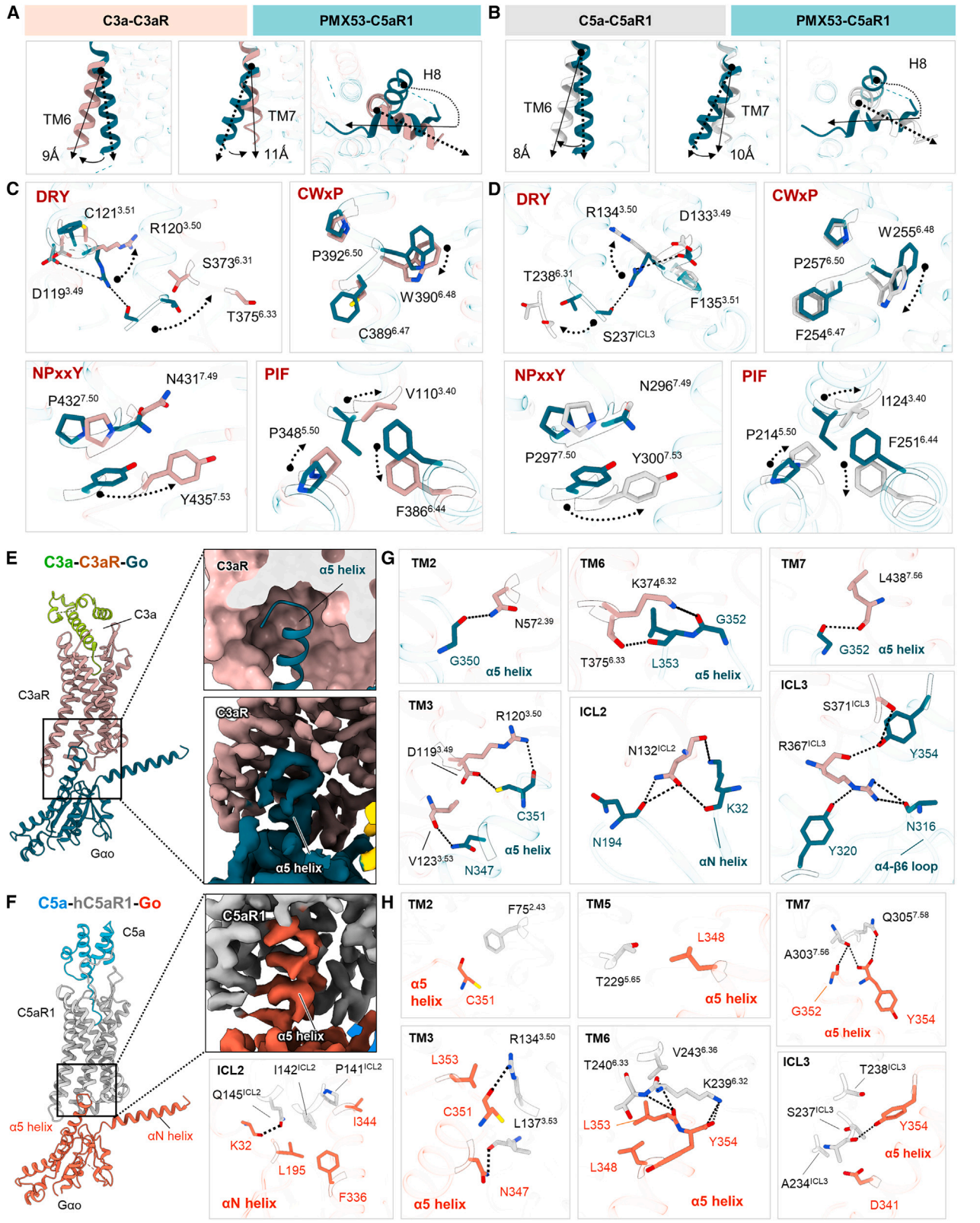

(legend on next page)

transducer-coupling response at C5aR1, C5a exhibited some cross-reactivity with C3aR, albeit only at moderately high concentration (i.e., 1 μM) in the G-protein-coupling assay (Figure 7A). More importantly, a pentadecameric peptide referred to as EP141 that is derived from and modified based on the carboxyl terminus sequence of C3a (Figure S7E) showed full efficacy for C3aR in G-protein-coupling assay, although it has lower potency compared with C3a (EC50 for C3a vs. EP141, ∼1.5 vs. 90 nM). On the other hand, it displays only partial efficacy in βarr-recruitment assay compared with C3a (Emax for EP141, ∼55%–65% of C3a) and lower potency (EC50 for C3a vs. EP141, ∼10–20 nM vs. ∼300–500 nM) (Figure 7A). In addition, although EP54 binds to both C3aR and C5aR1, EP141 is selective for C3aR (Figure 7A). The analysis of EP141 responses in G-protein and βarr1/2-recruitment assays yields a bias factor of ∼0.5 ± 0.05 (Figure 7A). We also tested EP141 using human monocyte-derived macrophages (HMDMs) and observed that it is a full agonist in terms of intracellular Ca^{2+} response, but unlike C3a, it does not attenuate lipopolysaccharide (LPS)-induced tumor necrosis factor alpha (TNF-α) and interleukin (IL)-6 secretion (Figure 7B). Interestingly, EP141 stimulation of HMDMs leads to an even higher ERK1/2 MAP kinase response than C3a (Figure 7B). This is particularly intriguing as previous studies have suggested that, unlike other GPCRs, βarrs play an inhibitory role in C3aR-induced ERK1/2 phosphorylation,[12,13] and therefore, lower efficacy of EP141 in terms of βarr recruitment may underlie the enhanced ERK response observed. In order to understand the molecular basis of G-protein bias exhibited by EP141, we reconstituted and determined the structure of EP141-C3aR-Go complex (Figures 7C, S2H, S4E, and S5; Tables S1 and S2). We observed that similar to the carboxyl terminus of C3a and EP54, EP141 also adopts a hook-like conformation to position itself in the orthosteric binding pocket, albeit it is aligned a little differently than EP54 (Figure 7D). Although EP141 exhibits extensive interactions in the orthosteric pocket, similar to those displayed by the analogous residues of C3a and EP54, including the contacts made by terminal Arg^{74}, it also displays additional interactions through Arg^{69} that were not previously observed. As presented in Figure 7E, Arg^{69} in EP141 forms a hydrogen bond network with $Ser400^{6.58}$, $Thr403^{6.61}$, and $Asp404^{ECL3}$ of the C3aR. These interactions result in an outward movement of the extracellular portions of TM6 and TM7 in C3aR by approximately 1.5 and 2.8 Å, respectively, and also a shift in ECL3 compared with C3a-bound C3aR (Figure 7F). It is interesting to note that Arg^{69} in C3a is a part of an α helix (H4), and thus, perhaps it is structurally constrained and unable to engage in hydrogen bond networks in a fashion similar to EP141. On the other hand, EP54 contains a lysine at the corresponding position that attains an alternative rotameric conformation, which precludes the possibility of it engaging in the same hydrogen bonding network as EP141. Considering the partial efficacy of EP141 in βarr assays compared with EP54 while maintaining similar potency and efficacy in terms of cAMP response, the structural observations presented here now lay a foundation to rationally design and optimize signaling-biased peptide agonists of C3aR. Taken together, these observations identify EP141 as a C3aR-selective, G-protein-biased agonist and provide a framework for designing additional biased agonists at C3aR. Considering the striking selectivity of EP141 for C3aR, even more than that displayed by C5a, it should allow the delineation of receptor subtype-selective cellular and physiological responses observed upon complement activation, and therefore, it may help refine the precise therapeutic window of selectively blocking the complement receptors. Moreover, these findings also underscore EP141 as a valuable tool compound to decipher the intricate details of biased agonism at C3aR and investigate the physiological outcomes of biased signaling at C3aR that has remained mostly unexplored.

DISCUSSION

The structural snapshots presented here provide the mechanistic basis of C3a and C5a recognition by their cognate receptors, C3aR and C5aR1, and elucidate previously unanticipated distinct binding modes of these anaphylatoxins to these receptors (Figure 7G). Importantly, we also uncover the molecular mechanism that allows the carboxyl-terminal peptide fragments of C3a and C5a to bind and activate C3aR and C5aR1, including the identification of a G-protein-biased agonist at C3aR, which illuminates intricate details of the so-called effector sites on these receptors sufficient for driving downstream functional responses. Moreover, these structures also offer previously lacking templates to facilitate structure-guided ligand discovery with subtype-selective pharmacology and signaling bias, and therefore, taken together with recent studies,[47,48] they should allow us to overcome a major limitation that has previously stunted the discovery of potential therapeutic molecules targeting the complement receptor in inflammatory disorders. It is also interesting to note that both C3aR and C5aR1 recruit βarrs; however, they appear to have distinct contributions in downstream signaling for these two receptors. For example, βarrs play an inhibitory role in agonist-induced ERK1/2 MAP kinase activation

Figure 6. Mechanism of activation and G-protein coupling at C3aR and C5aR1

(A and B) Dynamic changes in TMs of activated C3aR/C5aR1 compared with the inactive state of C5aR1. The TM6, TM7, and H8 from different receptor complexes shown are from receptors mentioned in boxes. Solid lines (active receptors) and dotted lines (inactive C5aR1) indicate direction of movement. The respective degrees of movements in corresponding TMs have also been mentioned.

(C and D) Close-up views of the conserved DRY, NPxxY, CWxP, and PIF motifs show conformational changes upon C3aR and C5aR1 activation. The names of the hallmark microswitches are noted inside respective boxes. Polar contacts are depicted as black dashed lines.

(E and F) α5 helix of Gαo docks into the cytoplasmic core of C3aR and C5aR1. Only receptor and Gαo are shown in ribbon representations to highlight the binding pose of G proteins with receptor core. Surface slice presentations (top) and cryo-EM maps are shown in inset boxes to highlight the direct docking of Gα to receptors.

(G and H) Magnified view of the interactions between TM2, TM3, TM6, TM7, ICL2, and ICL3 of C3aR and hC5aR1 with Gαo. Ionic bonds are depicted as black dashed lines.

See also Figures S4, S5, S6, and S7 and Table S2.

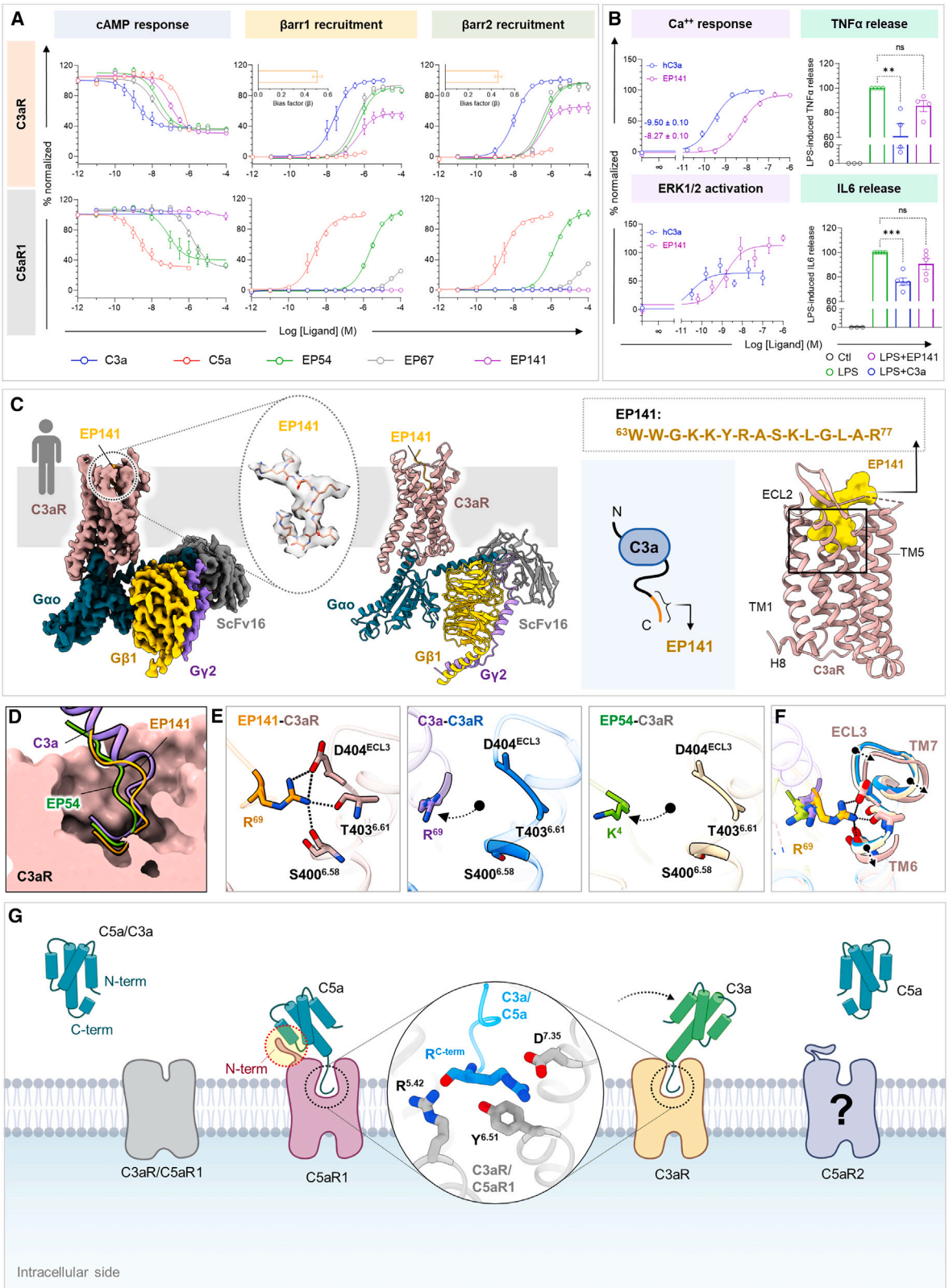

(legend on next page)

for C3aR[12,13] but a supportive role in the case of C5aR1.[40] Additionally, the second C5a receptor, C5aR2, selectively recruits βarrs without any measurable G-protein-dependent second messenger response, which makes it an example of intrinsically βarr-biased 7TMR.[40] Still, however, the structural basis of this unique functional manifestation by C5aR2 remains elusive, and therefore, future studies focused on this receptor are required to complete the molecular understanding of complement signaling through 7TMRs (Figure 7G). Taken together, these three complement receptors make a fascinating model system to decipher the intricate details of 7TMR-βarr interaction with distinct functional outcomes.

As mentioned earlier, excessive complement activation is linked to many diseases, and therefore, it continues to remain an important therapeutic area. For example, a small-molecule inhibitor of C5aR1 has recently been approved by the United States Food and Drug Administration for anti-neutrophil cytoplasmic antibody vasculitis (ANCA-vasculitis),[49] and a monoclonal antibody, marketed under the brand name Gohibic, targeting C5a to block its interaction with C5aR1, has been approved for use in hospitalized patients of COVID-19.[23] Moreover, a cyclic peptide inhibitor of complement C3 has also been approved for paroxysmal nocturnal hemoglobinuria (PNH)[50] and age-related macular degeneration (AMD).[51] However, the complement cascade also plays numerous roles in host protective mechanisms. For example, in a mouse model, C5a-C5aR1 interaction appears to contribute to the clearance of *Candida albicans* and improved host survival.[52] Furthermore, although C3a and C5a are broadly labeled as pro-inflammatory, there is now an appreciation that, unlike C5a, C3a exerts many immune-protective activities in the host. For example, following acute organ injury or infection, complement-mediated production of C3a confers protection in the brain, kidney, vessels, and intestine.[53–56] The development of biased ligands for C3a and C5a receptors may therefore allow for the specific protective activities of these receptors to be separated from their pathogenic activities. Indeed, our recent study demonstrates that EP141, the G-protein-biased agonist for C3aR identified here, can protect against tissue injury in a mouse ischemia reperfusion injury model.[53] In addition, we have also demonstrated previously that $C5a^{pep}$, a G-protein-biased agonist for C5aR1, attenuates LPS-mediated cytokine production from macrophages similar to C5a while exhibiting diminished pro-inflammatory response of neutrophil migration.[40] We also note that cytokines such as TNF-α and IL-6 are linked to inflammatory diseases such as rheumatoid arthritis and Crohn's disease; however, these cytokines are also important for host defense, and current anti-TNF and anti-IL-6 therapies increase infection risk.[57] Our finding that the endogenous C3a response to these cytokines can be modulated by biased receptor ligands may assist in the development of therapies tuned for different aspects of complement receptor function. Collectively, these observations underscore the therapeutic potential for biased agonists targeting C3aR and C5aR1, and the structural and pharmacological data presented here now provides a framework for exploring this direction going forward.

Limitations of the study

We note that the rotation of H8 observed in the active state structures of C5aR1 presented here, compared with the previously determined crystal structure of antagonist-bound C5aR1, merits further studies to probe its functional significance with respect to receptor signaling and regulation. We also acknowledge that our study is focused primarily on understanding the

Figure 7. Identification of a biased agonist and schematic of complement recognition by C3aR and C5aR1

(A) G-protein activation and βarr1/2 recruitment were studied using GloSensor assay and NanoBiT-based assay (receptor-SmBiT + LgBiT-βarr1/2), respectively, first panel: forskolin-induced cAMP level downstream of C3aR in response to indicated ligands (mean ± SEM; n = 4; normalized with the lowest ligand concentration for each ligand as 100%); second panel: βarr1 recruitment to C3aR (mean ± SEM; n = 4); and third panel: βarr2 recruitment to C3aR (mean ± SEM; n = 3); normalized with the highest ligand concentration of C3a as 100% (top). G-protein activation and βarr1/2 recruitment downstream of C5aR1 in response to indicated ligands, first panel: forskolin-induced cAMP level decrease downstream of C5aR1 in response to indicated ligands (mean ± SEM; n = 5; normalized with the lowest concentration of each ligand as 100%), second panel: βarr1 recruitment to C5aR1 (mean ± SEM; n = 5) and third panel: βarr2 recruitment to C5aR1 (mean ± SEM; n = 4); normalized with the highest ligand concentration of C5a as 100% (bottom). Bias factors (β value) determined taking C3a as reference elucidate the G-protein-biased nature of EP141 have been shown in insets. Bias factor was calculated using https://biasedcalculator.shinyapps.io/calc/.

(B) Intracellular calcium response, ERK1/2 activation, cytokine release upon stimulation with C3a, and EP141 were studied in human macrophages. Top left: calcium response (mean ± SEM; n = 9, data were normalized to the bottom [0%] and top [100%] values of the C3a dose-response curve). Bottom left: ERK1/2 activation (mean ± SEM; n = 9, normalized to the peak C3a-induced response for that donor). For cytokine release, top right: TNF-α release (mean ± SEM; n = 4), and bottom right: IL-6 release (mean ± SEM; n = 5), data were normalized to the medium only (0%) and LPS (100%) triggered response, analyzed using two-way ANOVA, Tukey's multiple comparison test. The exact p values are as follows: for TNFα release, LPS vs. LPS+C3a: (p = 0.0066), LPS only vs. LPS+EP141: (p = 0.3947). For IL6 release, LPS vs. LPS+C3a: (p = 0.0002), LPS vs. LPS+EP141 (p = 0.1048) (**p < 0.01, ***p < 0.001, ns, non-significant).

(C) Cryo-EM density map and corresponding model of EP141-C3aR-Go. Cryo-EM density map of EP141 has been shown in gray dotted circles (left). Sequence of EP141 derived from the C terminus of C3a. Side view of EP141 (surface) bound to C3aR (ribbon).

(D) The ligand binding pocket has been shown as surface slice representation to highlight the positioning of C3a, EP54, and EP141 on C3aR (right).

(E) Unique residue contacts between EP141 and C3aR at the ligand binding pocket might help explain the phenotypic behavior exhibited by EP141. Arg^{69} of EP141 makes extensive interactions with residues from TM6 and ECL3 (left), which are absent in C3a-C3aR (middle) and EP54-C3aR complexes (right). Black dotted arrows represent probable movements of Arg^{69} in C3a and Lys^{4} in EP54 with respect to Arg^{69} in EP141.

(F) Interactions by Arg^{69} of EP141 with C3aR result in outward movements in TM6, TM7, and ECL3 in C3aR.

(G) Schematic diagram showing ligand binding of the complement receptors C3aR and C5aR1. The C-terminal tail of C3a/C5a changes its conformation to form a hook-like loop upon interacting with C3aR/C5aR1. In addition to the ECLs and the extracellular side of TMs of both the receptors, C5a engages with an extra interface on N terminus of C5aR1. Absence of this interaction network on N terminus might explain the differential positioning of C3a compared with C5a. A group of charged residues on C3aR/C5aR1 interact and stabilize the critical terminal Arg with polar contacts from the C terminus of complement peptides. C5a also binds to C5aR2, but the mechanism behind this interaction has yet to be explored in high detail.

See also Figures S1 and S7, Table S2, and Methods S1.

fundamental mechanism of complement anaphylatoxin recognition by their cognate receptors, and although it paves the way for structure-guided ligand discovery, it does not directly delve into such an exercise. In addition, we also note that this study is focused primarily on C3aR and C5aR1 and not on C5aR2, which remains to be explored in future studies with respect to complement C5a binding, activation, and its intrinsic βarr bias that we have described earlier.[15,40]

STAR★METHODS

Detailed methods are provided in the online version of this paper and include the following:

- KEY RESOURCES TABLE
- RESOURCE AVAILABILITY
  - Lead contact
  - Materials availability
  - Data and code availability
- EXPERIMENTAL MODEL AND STUDY PARTICIPANT DETAILS
  - Human cell line
  - Human monocyte cell-derived macrophages (HMDMs)
  - Insect cell line
  - Bacterial cell culture
- METHOD DETAILS
  - General chemicals, plasmids, and cell culture
  - GloSensor-based cAMP assay
  - Surface expression assay
  - NanoBiT-based βarr-recruitment assay
  - Agonist-induced endosomal trafficking of βarrs
  - Assays with HMDMs
  - Expression and purification of C3a and C3aR
  - Expression and purification of C5a, $C5a^{des\text{-}Arg}$, and C5aR1
  - Expression and purification of G proteins
  - Expression and purification of ScFv16
  - Reconstitution of the C3a/EP54/EP141-C3aR-Gαo/-Gαq-Gβγ-ScFv16 complexes
  - Reconstitution of the $C5a/C5a^{pep}$-C5aR1-Gαoβ1γ2-ScFv16 complexes
  - Single-particle, negative-stain electron microscopy
  - Cryo-EM grid preparation and data collection
  - Image processing and map construction
  - Model building and refinement
- QUANTIFICATION AND STATISTICAL ANALYSIS

SUPPLEMENTAL INFORMATION

Supplemental information can be found online at https://doi.org/10.1016/j.cell.2023.09.020.

ACKNOWLEDGMENTS

This work is supported primarily by the Science and Engineering Research Board (IPA/2020/000405 and SPR/2020/000408), an extramural grant from the Department of Biotechnology (DBT) (BT/PR29041/BRB/10/1697/2018) sanctioned under the Membrane Protein Structural Biology initiative, and the National Bioscience Award (BT/HRD/NBA/39/06/2018-19). In addition, the research in A.K.S.'s laboratory is supported by the Senior Fellowship of the DBT Wellcome Trust India Alliance (IA/S/20/1/504916) awarded to A.K.S., the Council of Scientific and Industrial Research (37(1730)/19/EMR-II), the Indian Council of Medical Research (F.NO.52/15/2020/BIO/BMS), the Young Scientist Award from the Lady Tata Memorial Trust, and IIT Kanpur. A.K.S. is an EMBO Young Investigator. Shirsha Saha is supported by the Prime Minister's Research Fellowship. This research was also supported by a US National Institutes of Health grant R01 GM144965 (to C.G.). T.M.W. acknowledges support from the National Health and Medical Research Council (2009957). We also thank Mithu Baidya for the construct design of mC5aR1; Minakshi Baruah for initial purification ScFv16; Ashutosh Ranjan for assistance in purification of C5a; Bhanupriya Panigrahi, Saloni Sharma, and Gargi Mahajan for helping with protein purification; and Annu Dalal and Nashrah Zaidi for assistance with some functional assays. We thank T. Osinski at the USC Center for Advanced Research Computing (CARC) for support with computing resources. We acknowledge the Center of Excellence for Nano Imaging (CNI) at the University of Southern California for microscope time. Cryo-EM on mC5aR1 was performed at the BioEM lab of the Biozentrum at the University of Basel, and we thank Carola Alampi and David Kalbermatter for their excellent technical assistance.

AUTHOR CONTRIBUTIONS

M.K.Y. expressed and purified C3aR and hC5aR1 and reconstituted the complex with G proteins for negative staining and cryo-EM. R.Y. carried out cryo-EM screening, data collection, and structure determination on C3aR and hC5aR1 complexes. J.M. and R.B. carried out negative staining on the complexes, participated in data processing, structure determination, and analyzed the structures. Shirsha Saha and M.K.Y. expressed and purified mC5aR1 and reconstituted the complex with G proteins for negative staining and cryo-EM, and Shirsha Saha carried out the functional assays on C5aR1 with help from P.S. P.S. generated all the constructs for functional assays on C3aR and performed the cellular assays with help from C.S. and Shirsha Saha. C.S. started the expression, purification, and reconstitution of C3aR complexes including purification of G proteins and C3a. V.S. and Sayantan Saha contributed to the purification of G proteins, C3a, C5a, and ScFv16 and also assisted with reconstitution and purification of the complexes. S. Mohapatra and S. Mishra contributed to purification of ScFv16 and C5a. H.A.K. assisted with data collection on C3aR and hC5aR1 complexes. M.C. prepared the grids and collected cryo-EM data on mC5aR1 complexes. X.X.L. and T.M.W. designed and performed the HMDM assays. J.M. prepared all the figures with inputs from R.B., M.K.Y., R.Y., Shirsha Saha, P.S., and M.G. A.K.S. and C.G. supervised and managed the overall project. All authors contributed to data analysis, interpretation, and manuscript writing.

DECLARATION OF INTERESTS

The authors declare no competing interests.

INCLUSION AND DIVERSITY

We support inclusive, diverse, and equitable conduct of research.

Received: February 15, 2023
Revised: July 19, 2023
Accepted: September 20, 2023
Published: October 17, 2023

REFERENCES

1. Ember, J.A., and Hugli, T.E. (1997). Complement factors and their receptors. Immunopharmacology *38*, 3–15. https://doi.org/10.1016/s0162-3109(97)00088-x.
2. Sarma, J.V., and Ward, P.A. (2011). The complement system. Cell Tissue Res. *343*, 227–235. https://doi.org/10.1007/s00441-010-1034-0.
3. Merle, N.S., Church, S.E., Fremeaux-Bacchi, V., and Roumenina, L.T. (2015). Complement System Part I - Molecular Mechanisms of Activation

and Regulation. Front. Immunol. *6*, 262. https://doi.org/10.3389/fimmu.2015.00262.

4. Merle, N.S., Noe, R., Halbwachs-Mecarelli, L., Fremeaux-Bacchi, V., and Roumenina, L.T. (2015). Complement System Part II: Role in Immunity. Front. Immunol. *6*, 257. https://doi.org/10.3389/fimmu.2015.00257.
5. Hawksworth, O.A., Li, X.X., Coulthard, L.G., Wolvetang, E.J., and Woodruff, T.M. (2017). New concepts on the therapeutic control of complement anaphylatoxin receptors. Mol. Immunol. *89*, 36–43. https://doi.org/10.1016/j.molimm.2017.05.015.
6. Hawksworth, O.A., Coulthard, L.G., Mantovani, S., and Woodruff, T.M. (2018). Complement in stem cells and development. Semin. Immunol. *37*, 74–84. https://doi.org/10.1016/j.smim.2018.02.009.
7. Hawksworth, O.A., Coulthard, L.G., and Woodruff, T.M. (2017). Complement in the fundamental processes of the cell. Mol. Immunol. *84*, 17–25. https://doi.org/10.1016/j.molimm.2016.11.010.
8. Klos, A., Wende, E., Wareham, K.J., and Monk, P.N. (2013). International Union of Basic and Clinical Pharmacology. [corrected]. LXXXVII. Complement peptide C5a, C4a, and C3a receptors. Pharmacol. Rev. *65*, 500–543. https://doi.org/10.1124/pr.111.005223.
9. Monk, P.N., Scola, A.M., Madala, P., and Fairlie, D.P. (2007). Function, structure and therapeutic potential of complement C5a receptors. Br. J. Pharmacol. *152*, 429–448. https://doi.org/10.1038/sj.bjp.0707332.
10. Ames, R.S., Li, Y., Sarau, H.M., Nuthulaganti, P., Foley, J.J., Ellis, C., Zeng, Z., Su, K., Jurewicz, A.J., Hertzberg, R.P., et al. (1996). Molecular cloning and characterization of the human anaphylatoxin C3a receptor. J. Biol. Chem. *271*, 20231–20234. https://doi.org/10.1074/jbc.271.34.20231.
11. Pandey, S., Maharana, J., Li, X.X., Woodruff, T.M., and Shukla, A.K. (2020). Emerging insights into the structure and function of complement C5a receptors. Trends Biochem. Sci. *45*, 693–705. https://doi.org/10.1016/j.tibs.2020.04.004.
12. Guo, Q., Subramanian, H., Gupta, K., and Ali, H. (2011). Regulation of C3a receptor signaling in human mast cells by G protein coupled receptor kinases. PLoS One *6*, e22559. https://doi.org/10.1371/journal.pone.0022559.
13. Vibhuti, A., Gupta, K., Subramanian, H., Guo, Q., and Ali, H. (2011). Distinct and shared roles of beta-arrestin-1 and beta-arrestin-2 on the regulation of C3a receptor signaling in human mast cells. PLoS One *6*, e19585. https://doi.org/10.1371/journal.pone.0019585.
14. Gupta, K., Subramanian, H., Klos, A., and Ali, H. (2012). Phosphorylation of C3a receptor at multiple sites mediates desensitization, beta-arrestin-2 recruitment and inhibition of NF-kappaB activity in mast cells. PLoS One *7*, e46369. https://doi.org/10.1371/journal.pone.0046369.
15. Pandey, S., Kumari, P., Baidya, M., Kise, R., Cao, Y., Dwivedi-Agnihotri, H., Banerjee, R., Li, X.X., Cui, C.S., Lee, J.D., et al. (2021). Intrinsic bias at non-canonical, beta-arrestin-coupled seven transmembrane receptors. Mol. Cell *81*, 4605–4621.e11. https://doi.org/10.1016/j.molcel.2021.09.007.
16. Croker, D.E., Monk, P.N., Halai, R., Kaeslin, G., Schofield, Z., Wu, M.C.L., Clark, R.J., Blaskovich, M.A.T., Morikis, D., Floudas, C.A., et al. (2016). Discovery of functionally selective C5aR2 ligands: novel modulators of C5a signalling. Immunol. Cell Biol. *94*, 787–795. https://doi.org/10.1038/icb.2016.43.
17. Croker, D.E., Halai, R., Kaeslin, G., Wende, E., Fehlhaber, B., Klos, A., Monk, P.N., and Cooper, M.A. (2014). C5a2 can modulate ERK1/2 signaling in macrophages via heteromer formation with C5a1 and beta-arrestin recruitment. Immunol. Cell Biol. *92*, 631–639. https://doi.org/10.1038/icb.2014.32.
18. Peng, Q., Li, K., Wang, N., Li, Q., Asgari, E., Lu, B., Woodruff, T.M., Sacks, S.H., and Zhou, W. (2009). Dendritic cell function in allostimulation is modulated by C5aR signaling. J. Immunol. *183*, 6058–6068. https://doi.org/10.4049/jimmunol.0804186.
19. Muenstermann, M., Strobel, L., Klos, A., Wetsel, R.A., Woodruff, T.M., Köhl, J., and Johswich, K.O. (2019). Distinct roles of the anaphylatoxin receptors C3aR, C5aR1 and C5aR2 in experimental meningococcal infections. Virulence *10*, 677–694. https://doi.org/10.1080/21505594.2019.1640035.
20. Muenstermann, M., Herrmann, J., Strobel, L., Woodruff, T., Klos, A., Wetsel, R., Gerard, C., Köhl, J., and Johswich, K.O. (2018). The distinct roles of the anaphylatoxin receptors C5aR1, C5aR2 and C3aR during experimental invasive meningococcal disease. Mol. Immunol. *102*, 168–169. https://doi.org/10.1016/j.molimm.2018.06.109.
21. Wetsel, R.A. (1995). Structure, function and cellular expression of complement anaphylatoxin receptors. Curr. Opin. Immunol. *7*, 48–53. https://doi.org/10.1016/0952-7915(95)80028-x.
22. Carvelli, J., Demaria, O., Vély, F., Batista, L., Benmansour, N.C., Fares, J., Carpentier, S., Thibult, M.L., Morel, A., Remark, R., et al. (2020). Association of COVID-19 inflammation with activation of the C5a-C5aR1 axis. Nature *588*, 146–150. https://doi.org/10.1038/s41586-020-2600-6.
23. Vlaar, A.P.J., Witzenrath, M., van Paassen, P., Heunks, L.M.A., Mourvillier, B., de Bruin, S., Lim, E.H.T., Brouwer, M.C., Tuinman, P.R., Saraiva, J.F.K., et al. (2022). Anti-C5a antibody (vilobelimab) therapy for critically ill, invasively mechanically ventilated patients with COVID-19 (PANAMO): a multicentre, double-blind, randomised, placebo-controlled, phase 3 trial. Lancet Respir. Med. *10*, 1137–1146. https://doi.org/10.1016/S2213-2600(22)00297-1.
24. Bajic, G., Yatime, L., Klos, A., and Andersen, G.R. (2013). Human C3a and C3a desArg anaphylatoxins have conserved structures, in contrast to C5a and C5a desArg. Protein Sci. *22*, 204–212. https://doi.org/10.1002/pro.2200.
25. Schatz-Jakobsen, J.A., Yatime, L., Larsen, C., Petersen, S.V., Klos, A., and Andersen, G.R. (2014). Structural and functional characterization of human and murine C5a anaphylatoxins. Acta Crystallogr. D Biol. Crystallogr. *70*, 1704–1717. https://doi.org/10.1107/S139900471400844X.
26. Sun, J.Z., Ember, J.A., Chao, T.H., Fukuoka, Y., Ye, R.D., and Hugli, T.E. (1999). Identification of ligand effector binding sites in transmembrane regions of the human G protein-coupled C3a receptor. Protein Sci. *8*, 2304–2311.
27. Chao, T.H., Ember, J.A., Wang, M., Bayon, Y., Hugli, T.E., and Ye, R.D. (1999). Role of the second extracellular loop of human C3a receptor in agonist binding and receptor function. J. Biol. Chem. *274*, 9721–9728. https://doi.org/10.1074/jbc.274.14.9721.
28. Siciliano, S.J., Rollins, T.E., DeMartino, J., Konteatis, Z., Malkowitz, L., Van Riper, G., Bondy, S., Rosen, H., and Springer, M.S. (1994). Two-site binding of C5a by its receptor: an alternative binding paradigm for G protein-coupled receptors. Proc. Natl. Acad. Sci. USA *91*, 1214–1218. https://doi.org/10.1073/pnas.91.4.1214.
29. DeMartino, J.A., Van Riper, G., Siciliano, S.J., Molineaux, C.J., Konteatis, Z.D., Rosen, H., and Springer, M.S. (1994). The amino terminus of the human C5a receptor is required for high affinity C5a binding and for receptor activation by C5a but not C5a analogs. J. Biol. Chem. *269*, 14446–14450.
30. Vogen, S.M., Prakash, O., Kirnarsky, L., Sanderson, S.D., and Sherman, S.A. (1999). Determination of structural elements related to the biological activities of a potent decapeptide agonist of human C5a anaphylatoxin. J. Pept. Res. *54*, 74–84. https://doi.org/10.1034/j.1399-3011.1999.00087.x.
31. Vogen, S.M., Paczkowski, N.J., Kirnarsky, L., Short, A., Whitmore, J.B., Sherman, S.A., Taylor, S.M., and Sanderson, S.D. (2001). Differential activities of decapeptide agonists of human C5a: the conformational effects of backbone N-methylation. Int. Immunopharmacol. *1*, 2151–2162. https://doi.org/10.1016/S1567-5769(01)00141-2.
32. Halai, R., Bellows-Peterson, M.L., Branchett, W., Smadbeck, J., Kieslich, C.A., Croker, D.E., Cooper, M.A., Morikis, D., Woodruff, T.M., Floudas, C.A., and Monk, P.N. (2014). Derivation of ligands for the complement C3a receptor from the C-terminus of C5a. Eur. J. Pharmacol. *745*, 176–181. https://doi.org/10.1016/j.ejphar.2014.10.041.
33. Li, X.X., Clark, R.J., and Woodruff, T.M. (2021). Anaphylatoxin receptor promiscuity for commonly used complement C5a peptide agonists. Int.

Immunopharmacol. *100*, 108074. https://doi.org/10.1016/j.intimp.2021.108074.

34. Erickson, B.W., Tippett, P.S., and Hugli, T.E. (1977). Shortest active synthetic peptide from human C3a anaphylatoxin. Fed. Proc. *36*, 742.
35. Caporale, L.H., Tippett, P.S., Erickson, B.W., and Hugli, T.E. (1980). The active-site of C3a anaphylatoxin. J. Biol. Chem. *255*, 10758–10763.
36. Hugli, T.E. (1990). Structure and function of C3a anaphylatoxin. Curr. Top Microbiol. *153*, 181–208.
37. Scully, C.C.G., Blakeney, J.S., Singh, R., Hoang, H.N., Abbenante, G., Reid, R.C., and Fairlie, D.P. (2010). Selective hexapeptide agonists and antagonists for human complement C3a receptor. J. Med. Chem. *53*, 4938–4948. https://doi.org/10.1021/jm1003705.
38. Singh, R., Reed, A.N., Chu, P.F., Scully, C.C.G., Yau, M.K., Suen, J.Y., Durek, T., Reid, R.C., and Fairlie, D.P. (2015). Potent complement C3a receptor agonists derived from oxazole amino acids: Structure-activity relationships. Bioorg. Med. Chem. Lett. *25*, 5604–5608. https://doi.org/10.1016/j.bmcl.2015.10.038.
39. Li, X.X., Lee, J.D., Massey, N.L., Guan, C., Robertson, A.A.B., Clark, R.J., and Woodruff, T.M. (2020). Pharmacological characterisation of small molecule C5aR1 inhibitors in human cells reveals biased activities for signalling and function. Biochem. Pharmacol. *180*, 114156. https://doi.org/10.1016/j.bcp.2020.114156.
40. Pandey, S., Li, X.X., Srivastava, A., Baidya, M., Kumari, P., Dwivedi, H., Chaturvedi, M., Ghosh, E., Woodruff, T.M., and Shukla, A.K. (2019). Partial ligand-receptor engagement yields functional bias at the human complement receptor, C5aR1. J. Biol. Chem. *294*, 9416–9429. https://doi.org/10.1074/jbc.RA119.007485.
41. Wilken, H.C., Götze, O., Werfel, T., and Zwirner, J. (1999). C3a(desArg) does not bind to and signal through the human C3a receptor. Immunol. Lett. *67*, 141–145. https://doi.org/10.1016/S0165-2478(99)00002-4.
42. Polley, M.J., and Nachman, R.L. (1983). Human-platelet activation by C3a and C3a Des-Arg. Immunobiology *164*, 319.
43. Croker, D.E., Halai, R., Fairlie, D.P., and Cooper, M.A. (2013). C5a, but not C5a-des Arg, induces upregulation of heteromer formation between complement C5a receptors C5aR and C5L2. Immunol. Cell Biol. *91*, 625–633. https://doi.org/10.1038/icb.2013.48.
44. Croker, D.E., Halai, R., Fairlie, D.P., and Cooper, M.A. (2012). Ligand-induced dimerisation of the complement C5aR and C5L2 receptors by C5a but not C5a-des Arg. Immunobiology *217*, 1181–1182. https://doi.org/10.1016/j.imbio.2012.08.152.
45. Liu, H., Kim, H.R., Deepak, R.N.V.K., Wang, L., Chung, K.Y., Fan, H., Wei, Z., and Zhang, C. (2018). Orthosteric and allosteric action of the C5a receptor antagonists. Nat. Struct. Mol. Biol. *25*, 472–481. https://doi.org/10.1038/s41594-018-0067-z.
46. Robertson, N., Rappas, M., Doré, A.S., Brown, J., Bottegoni, G., Koglin, M., Cansfield, J., Jazayeri, A., Cooke, R.M., and Marshall, F.H. (2018). Structure of the complement C5a receptor bound to the extra-helical antagonist NDT9513727. Nature *553*, 111–114. https://doi.org/10.1038/nature25025.
47. Wang, Y., Liu, W., Xu, Y., He, X., Yuan, Q., Luo, P., Fan, W., Zhu, J., Zhang, X., Cheng, X., et al. (2023). Revealing the signaling of complement receptors C3aR and C5aR1 by anaphylatoxins. Nat. Chem. Biol. https://doi.org/10.1038/s41589-023-01339-w.
48. Feng, Y., Zhao, C., Deng, Y., Wang, H., Ma, L., Liu, S., Tian, X., Wang, B., Bin, Y., Chen, P., et al. (2023). Mechanism of activation and biased signaling in complement receptor C5aR1. Cell Res. *33*, 312–324. https://doi.org/10.1038/s41422-023-00779-2.
49. McGovern, D., Jones, R.B., Willcocks, L.C., Smith, R.M., Jayne, D.R.W., and Kronbichler, A. (2023). Avacopan for ANCA-associated vasculitis - information for prescribers. Nephrol. Dial. Transplant. *38*, 1067–1070. https://doi.org/10.1093/ndt/gfac330.
50. Rother, R.P., Rollins, S.A., Mojcik, C.F., Brodsky, R.A., and Bell, L. (2007). Discovery and development of the complement inhibitor eculizumab for the treatment of paroxysmal nocturnal hemoglobinuria. Nat. Biotechnol. *25*, 1256–1264. https://doi.org/10.1038/nbt1344.
51. Qin, S., Dong, N., Yang, M., Wang, J., Feng, X., and Wang, Y. (2021). Complement inhibitors in age-related macular degeneration: A potential therapeutic option. J. Immunol. Res. *2021*, 9945725. https://doi.org/10.1155/2021/9945725.
52. Desai, J.V., Kumar, D., Freiwald, T., Chauss, D., Johnson, M.D., Abers, M.S., Steinbrink, J.M., Perfect, J.R., Alexander, B., Matzaraki, V., et al. (2023). C5a-licensed phagocytes drive sterilizing immunity during systemic fungal infection. Cell *186*, 2802–2822.e22. https://doi.org/10.1016/j.cell.2023.04.031.
53. Wu, M.C., Brennan, F.H., Lynch, J.P., Mantovani, S., Phipps, S., Wetsel, R.A., Ruitenberg, M.J., Taylor, S.M., and Woodruff, T.M. (2013). The receptor for complement component C3a mediates protection from intestinal ischemia-reperfusion injuries by inhibiting neutrophil mobilization. Proc. Natl. Acad. Sci. USA *110*, 9439–9444. https://doi.org/10.1073/pnas.1218815110.
54. Brennan, F.H., Jogia, T., Gillespie, E.R., Blomster, L.V., Li, X.X., Nowlan, B., Williams, G.M., Jacobson, E., Osborne, G.W., Meunier, F.A., et al. (2019). Complement receptor C3aR1 controls neutrophil mobilization following spinal cord injury through physiological antagonism of CXCR2. JCI Insight *4*, e98254. https://doi.org/10.1172/jci.insight.98254.
55. Wei, L.L., Ma, N., Wu, K.Y., Wang, J.X., Diao, T.Y., Zhao, S.J., Bai, L., Liu, E.Q., Li, Z.F., Zhou, W.D., et al. (2020). Protective role of C3aR (C3a anaphylatoxin receptor) against atherosclerosis in atherosclerosis-prone mice. Arterioscler. Thromb. Vasc. Biol. *40*, 2070–2083. https://doi.org/10.1161/ATVBAHA.120.314150.
56. Zhao, S.J., Wu, K.Y., Min, X.Y., Wang, C.X., Cao, B., Ma, N., Yang, X.L., Zhu, Z.R., Fu, R.G., Zhou, W.D., et al. (2022). Protective role for C3aR in experimental chronic pyelonephritis. FASEB J. *36*, e22599. https://doi.org/10.1096/fj.202201007R.
57. Rose-John, S., Winthrop, K., and Calabrese, L. (2017). The role of IL-6 in host defence against infections: immunobiology and clinical implications. Nat. Rev. Rheumatol. *13*, 399–409. https://doi.org/10.1038/nrrheum.2017.83.
58. Zhu, Y., Lin, X., Zong, X., Han, S., Wang, M., Su, Y., Ma, L., Chu, X., Yi, C., Zhao, Q., et al. (2022). Structural basis of FPR2 in recognition of Abeta(42) and neuroprotection by humanin. Nat. Commun. *13*, 1775. https://doi.org/10.1038/s41467-022-29361-x.
59. Maeda, S., Qu, Q., Robertson, M.J., Skiniotis, G., and Kobilka, B.K. (2019). Structures of the M1 and M2 muscarinic acetylcholine receptor/G-protein complexes. Science *364*, 552–557. https://doi.org/10.1126/science.aaw5188.
60. Colley, C.S., Popovic, B., Sridharan, S., Debreczeni, J.E., Hargeaves, D., Fung, M., An, L.L., Edwards, B., Arnold, J., England, E., et al. (2018). Structure and characterization of a high affinity C5a monoclonal antibody that blocks binding to C5aR1 and C5aR2 receptors. mAbs *10*, 104–117. https://doi.org/10.1080/19420862.2017.1384892.
61. Zivanov, J., Otón, J., Ke, Z., von Kügelgen, A., Pyle, E., Qu, K., Morado, D., Castaño-Díez, D., Zanetti, G., Bharat, T.A.M., et al. (2022). A Bayesian approach to single-particle electron cryo-tomography in RELION-4.0. eLife *11*, e83724. https://doi.org/10.7554/eLife.83724.
62. Zivanov, J., Nakane, T., and Scheres, S.H.W. (2020). Estimation of high-order aberrations and anisotropic magnification from cryo-EM data sets in RELION-3.1. IUCrJ *7*, 253–267. https://doi.org/10.1107/S2052252520000081.
63. Zivanov, J., Nakane, T., Forsberg, B.O., Kimanius, D., Hagen, W.J., Lindahl, E., and Scheres, S.H. (2018). New tools for automated high-resolution cryo-EM structure determination in RELION-3. eLife *7*, e42166. https://doi.org/10.7554/eLife.42166.
64. Punjani, A., Rubinstein, J.L., Fleet, D.J., and Brubaker, M.A. (2017). cryoSPARC: algorithms for rapid unsupervised cryo-EM structure determination. Nat. Methods *14*, 290–296. https://doi.org/10.1038/nmeth.4169.

65. Pettersen, E.F., Goddard, T.D., Huang, C.C., Meng, E.C., Couch, G.S., Croll, T.I., Morris, J.H., and Ferrin, T.E. (2021). UCSF ChimeraX: Structure visualization for researchers, educators, and developers. Protein Sci. *30*, 70–82. https://doi.org/10.1002/pro.3943.

66. Pettersen, E.F., Goddard, T.D., Huang, C.C., Couch, G.S., Greenblatt, D.M., Meng, E.C., and Ferrin, T.E. (2004). UCSF Chimera–a visualization system for exploratory research and analysis. J. Comput. Chem. *25*, 1605–1612. https://doi.org/10.1002/jcc.20084.

67. Casañal, A., Lohkamp, B., and Emsley, P. (2020). Current developments in Coot for macromolecular model building of Electron Cryo-microscopy and Crystallographic Data. Protein Sci. *29*, 1069–1078. https://doi.org/10.1002/pro.3791.

68. Emsley, P., Lohkamp, B., Scott, W.G., and Cowtan, K. (2010). Features and development of Coot. Acta Crystallogr. D Biol. Crystallogr. *66*, 486–501. https://doi.org/10.1107/S0907444910007493.

69. Emsley, P., and Cowtan, K. (2004). Coot: model-building tools for molecular graphics. Acta Crystallogr. D Biol. Crystallogr. *60*, 2126–2132. https://doi.org/10.1107/S0907444904019158.

70. Liebschner, D., Afonine, P.V., Baker, M.L., Bunkóczi, G., Chen, V.B., Croll, T.I., Hintze, B., Hung, L.W., Jain, S., McCoy, A.J., et al. (2019). Macromolecular structure determination using X-rays, neutrons and electrons: recent developments in Phenix. Acta Crystallogr. D Struct. Biol. *75*, 861–877. https://doi.org/10.1107/S2059798319011471.

71. Adams, P.D., Afonine, P.V., Bunkóczi, G., Chen, V.B., Davis, I.W., Echols, N., Headd, J.J., Hung, L.W., Kapral, G.J., Grosse-Kunstleve, R.W., et al. (2010). PHENIX: a comprehensive Python-based system for macromolecular structure solution. Acta Crystallogr. D Biol. Crystallogr. *66*, 213–221. https://doi.org/10.1107/S0907444909052925.

72. Krissinel, E., and Henrick, K. (2007). Inference of macromolecular assemblies from crystalline state. J. Mol. Biol. *372*, 774–797. https://doi.org/10.1016/j.jmb.2007.05.022.

73. Laskowski, R.A., Jabłońska, J., Pravda, L., Vařeková, R.S., and Thornton, J.M. (2018). PDBsum: Structural summaries of PDB entries. Protein Sci. *27*, 129–134. https://doi.org/10.1002/pro.3289.

74. Kawakami, K., Yanagawa, M., Hiratsuka, S., Yoshida, M., Ono, Y., Hiroshima, M., Ueda, M., Aoki, J., Sako, Y., and Inoue, A. (2022). Heterotrimeric Gq proteins act as a switch for GRK5/6 selectivity underlying beta-arrestin transducer bias. Nat. Commun. *13*, 487. https://doi.org/10.1038/s41467-022-28056-7.

75. Dijon, N.C., Nesheva, D.N., and Holliday, N.D. (2021). Luciferase complementation approaches to measure GPCR signaling kinetics and bias. Methods Mol. Biol. *2268*, 249–274. https://doi.org/10.1007/978-1-0716-1221-7_17.

76. Baidya, M., Chaturvedi, M., Dwivedi-Agnihotri, H., Ranjan, A., Devost, D., Namkung, Y., Stepniewski, T.M., Pandey, S., Baruah, M., Panigrahi, B., et al. (2022). Allosteric modulation of GPCR-induced beta-arrestin trafficking and signaling by a synthetic intrabody. Nat. Commun. *13*, 4634. https://doi.org/10.1038/s41467-022-32386-x.

77. Baidya, M., Kumari, P., Dwivedi-Agnihotri, H., Pandey, S., Chaturvedi, M., Stepniewski, T.M., Kawakami, K., Cao, Y., Laporte, S.A., Selent, J., et al. (2020). Key phosphorylation sites in GPCRs orchestrate the contribution of beta-arrestin in ERK1/2 activation. EMBO Rep. *21*, e49886. https://doi.org/10.15252/embr.201949886.

78. Kumar, B.A., Kumari, P., Sona, C., and Yadav, P.N. (2017). GloSensor assay for discovery of GPCR-selective ligands. Methods Cell Biol. *142*, 27–50. https://doi.org/10.1016/bs.mcb.2017.07.012.

79. Pandey, S., Roy, D., and Shukla, A.K. (2019). Measuring surface expression and endocytosis of GPCRs using whole-cell ELISA. Methods Cell Biol. *149*, 131–140. https://doi.org/10.1016/bs.mcb.2018.09.014.

80. Maharana, J., Sarma, P., Yadav, M.K., Saha, S., Singh, V., Saha, S., Chami, M., Banerjee, R., and Shukla, A.K. (2023). Structural snapshots uncover a key phosphorylation motif in GPCRs driving beta-arrestin activation. Mol. Cell *83*, 2091–2107.e7. https://doi.org/10.1016/j.molcel.2023.04.025.

81. Dwivedi-Agnihotri, H., Sarma, P., Deeksha, S., Kawakami, K., Inoue, A., and Shukla, A.K. (2022). An intrabody sensor to monitor conformational activation of beta-arrestins. Methods Cell Biol. *169*, 267–278. https://doi.org/10.1016/bs.mcb.2021.12.023.

82. Petering, H., Köhl, J., Weyergraf, A., Dulkys, Y., Kimmig, D., Smolarski, R., Kapp, A., and Elsner, J. (2000). Characterization of synthetic C3a analog peptides on human eosinophils in comparison to the native complement component C3a. J. Immunol. *164*, 3783–3789. https://doi.org/10.4049/jimmunol.164.7.3783.

83. Nehmé, R., Carpenter, B., Singhal, A., Strege, A., Edwards, P.C., White, C.F., Du, H., Grisshammer, R., and Tate, C.G. (2017). Mini-G proteins: Novel tools for studying GPCRs in their active conformation. PLoS One *12*, e0175642. https://doi.org/10.1371/journal.pone.0175642.

84. Carpenter, B., and Tate, C.G. (2017). Expression and purification of mini G proteins from Escherichia coli. Bio Protoc. *7*, 7. https://doi.org/10.21769/BioProtoc.2235.

85. Hong, C., Byrne, N.J., Zamlynny, B., Tummala, S., Xiao, L., Shipman, J.M., Partridge, A.T., Minnick, C., Breslin, M.J., Rudd, M.T., et al. (2021). Structures of active-state orexin receptor 2 rationalize peptide and small-molecule agonist recognition and receptor activation. Nat. Commun. *12*, 815. https://doi.org/10.1038/s41467-021-21087-6.

STAR★METHODS

KEY RESOURCES TABLE

REAGENT or RESOURCE	SOURCE	IDENTIFIER
Antibodies		
Monoclonal ANTI-FLAG M2-HRP antibody	Sigma-Aldrich	Cat# A8592; RRID: AB_439702
Bacterial and virus strains		
E. coli strain BL21(DE3)	New England Biolabs	Cat# C2527H
E. coli strain SHuffle	New England Biolabs	Cat# C3028
E. coli strain Rosetta (DE3)	Sigma-Aldrich	Cat# 70954
Chemicals, peptides, and recombinant proteins		
TRIS	SRL	Cat# 71033
HEPES	SRL	Cat# 63732
NaCl	SRL	Cat# 41721
EDTA	SRL	Cat# 12070
Phenylmethanesulfonyl Fluoride (PMSF)	SRL	Cat# 84375
L-Cysteine Hydrochloride Monohydrate	Sigma Aldrich	Cat# C7880
Iodoacetamide	Sigma Aldrich	Cat# I1149
Imidazole	Sigma Aldrich	Cat# I202-500G
Benzamidine Hydrochloride	SRL	Cat# 93014 (0248255)
Lysozyme	SRL	Cat# 45822
Glycerol	SRL	Cat# 77453
Dithiothreitol	HiMedia	Cat# MB070
Lauryl Maltose Neopentyl Glycol (MNG)	Anatrace	Cat# NG310, CAS no.1257852-96-2
Dodecyl Maltoside (DDM)	Anatrace	Cat# D310A
Cholesteryl Hemisuccinate (CHS)	Sigma Aldrich	Cat# C6512
Paraformaldehyde (PFA)	Sigma Aldrich	Cat# P6148, CAS no. 30525-89-4
Poly-D-lysine	Sigma Aldrich	Cat# P0899
TMB (Tetramethylbenzidine)	Thermo Fisher Scientific	Cat# 34028
Janus Green B	Sigma Aldrich	Cat# 201677
PEI (Polyethylenimine)	Polysciences	Cat# 23966
Bovine Serum Albumin, BSA	SRL	Cat# 83803 (0140105)
FLAG peptide	GenScript	N/A
HBSS - Hank's Balanced Salt Solution	Thermo Fisher Scientific	Cat# 14065
GIBCO Fetal Bovine Serum	Thermo Fisher Scientific	Cat# 10270-106
Iscove's Modified Dulbecco's Medium	Thermo Fisher Scientific	Cat# 12440053
DMEM	Cellclone	Cat# CC3004
Phosphate-buffered saline (PBS)	Sigma Aldrich	Cat# D1283
GIBCO Penicillin-Streptomycin	Thermo Fisher Scientific	Cat# 15140122
ESF921 Insect Cell Culture Medium	Expression Systems	Cat#96-001-01
Coelenterazine	Goldbio	Cat# CZ05
D-Luciferin Sodium Salt	Goldbio	Cat# LUCNA-1G
Glyco-diosgenin (GDN)	Anatrace	GDN101
Coomassie Brilliant Blue	SRL	Cat# 64222
Uranyl formate	Polysciences	Cat# 24762-1
Apyrase	New England Biolabs	Cat# M0398S
Recombinant Gαo	This study	N/A
Recombinant Gαq	This study	N/A

(*Continued on next page*)

Continued

REAGENT or RESOURCE	SOURCE	IDENTIFIER
Recombinant Gβ1γ2 heterodimer	This study	N/A
Recombinant ScFv16	This study	N/A
Recombinant human C5a	This study	N/A
Recombinant mouse C5a	This study	N/A
Recombinant human C3a	This study	N/A
Recombinant human C5adesArg	This study	N/A
$C5a^{pep}$	GenScript	N/A
EP54	GenScript	N/A
EP67	GenScript	N/A
EP141	GenScript	N/A
Recombinant human macrophage colony stimulating factor	BioLegend, San Diego, USA	Cat# 574814
Formvar/carbon coated 300 mesh copper grids	PELCO (Ted Pella)	Cat# 01753-F
Critical commercial assays		
Site Directed Mutagenesis Kit	NEB	Cat# E0554
NanoBiT assay	Promega	N/A
GloSensor assay	Promega	N/A
BD OptEIA™ Human IL-6 ELISA Set	BD OptEIA	Cat# 555220
BD OptEIA™ Human TNF ELISA Set	BD OptEIA	Cat# 555221
Fluo-4 NW Calcium Assay Kit	Thermo Fisher Scientific	Cat# F36206
AlphaLISA SureFire Ultra p-ERK1/2 (Thr202/Tyr204) Assay Kit	Perkinelmer	Cat# ALSU-PERK-A-HV
Deposited data		
Apo-C3aR-Go complex (Glacios)	This study	PDB: 8I97, EMD-35259
Apo-C3aR-Go complex (Titan)	This study	PDB: 8I9S, EMD-35282
C3a-C3aR-Go complex (Composite map)	This study	PDB: 8I9L, EMD-35275
C3a-C3aR-Go (C3aR-Go complex only, Original Map)	This study	EMD-35293
C3a-C3aR-Go (C3a only, Original Map)	This study	EMD-35294
C5a-hC5aR1-Go (Composite map)	This study	PDB: 8IA2, EMD-35292
C5a-hC5aR1-Go (hC5aR1-Go complex only, original map)	This study	EMD-35295
C5a-hC5aR1-Go complex (C5a only, original map)	This study	EMD-35296
C5a-mC5aR1-Go	This study	PDB: 8HQC, EMD-34947
C5a-pep-mC5aR1-Go	This study	PDB: 8HPT, EMD-34943
EP141-C3aR-Go	This study	PDB: 8J6D, EMD-36001
EP54-C3aR-Go	This study	PDB: 8I95, EMD-35257
EP54-C3aR-Gq	This study	PDB: 8I9A, EMD-35263
C5a-desArg-hC5aR1-Go	This study	PDB: 8JZZ, EMD-36755
Crystal Structure of the Human C3a anaphylatoxin	Bajic et al.[24]	PDB: 4HW5
Human formyl peptide receptor 2 in complex with fMLFII and Gi2	Zhu et al.[58]	PDB:7WVV
Muscarinic acetylcholine receptor 2-Go complex	Maeda et al.[59]	PDB: 6OIK
Human c5a in complex with MEDI7814 a neutralizing antibody	Colley et al.[60]	PDB: 4UU9
Gel images and Functional assay data	This study	Mendeley data https://doi.org/10.17632/km5vft8gkd.1
Experimental models: Cell lines		
Human: HEK293	ATCC	Cat# CRL-3216
Human monocyte-derived macrophages (HMDM)	Australian Red Cross LifeBlood Service, Brisbane, Australia	N/A

(*Continued on next page*)

Continued

REAGENT or RESOURCE	SOURCE	IDENTIFIER
Spodoptera frugiperda (*Sf9*) Cell line	Expression Systems	Cat# 94-001F
Oligonucleotides		
mC5aR1 (wild type and mutants) cloning in pCAGGS vector_Forward: CGGGGTACCGAGGAGATCTGCCA CCATGGGCAAGACCATCATCGC	This study	N/A
mC5aR1 (wild type and mutants) cloning in pCAGGS vector_Reverse: TCCCCCGGGGACGGCCTGGGACT TGCG	This study	N/A
hC5aR1 cloning in pCAGGS vector_Forward: CGGGGTACCGAGGAGATCTGCCACCATGGGGAAG ACGATCATCGCC	This study	N/A
hC5aR1 cloning in pCAGGS vector_Reverse: TCCC CCGGGCACTGCCTGGGTC	This study	N/A
C3aR cloning in pCAGGS vector_Forward: CGGGGTACCGAGGAGATCTGCCACCATGGGGAA GACGATCATCGCC	This study	N/A
C3aR cloning in pCAGGS vector_Reverse: TCCCCCGGGCACTGTGGTAGAGTTTCTC	This study	N/A
mC5aR1_E176V SDM primer Forward: CGTGTACAGAgtgGCTTACAAGG	This study	N/A
mC5aR1_E176V SDM primer Reverse: AATGATGGGATAGTCAGCAG	This study	N/A
mC5aR1_Y178R SDM primer Forward: CAGAGAGGCTcgcAAGGACTTCTAC	This study	N/A
mC5aR1_Y178R SDM primer Reverse: TACACGAATGATGGGATAG	This study	N/A
mC5aR1_E280K SDM primer Forward: GAAGCGCGTGaagAAGCTGAACA	This study	N/A
mC5aR1_E280K SDM primer Reverse: AGAGTAGGGGATGAGGGAG	This study	N/A
mC5aR1_N283D SDM primer Forward: GGAGAAGCTGgacAGCCTGTGCG	This study	N/A
mC5aR1_N283D SDM primer Reverse: ACGCGCTTCAGAGTAGGG	This study	N/A
Recombinant DNA		
pCDNA_3.1 (empty vector)	Dr. Arun K Shukla	N/A
pcDNA3.1_hC5aR1	Dr. Arun K Shukla	N/A
pcDNA3.1_mC5aR1	This study	N/A
pcDNA3.1_C3aR	This study	N/A
pCAGGS_hC5aR1	This study	N/A
pCAGGS _mC5aR1	This study	N/A
pCAGGS _mC5aR1^{E176V}	This study	N/A
pCAGGS _mC5aR1^{Y178R}	This study	N/A
pCAGGS _mC5aR1^{E280K}	This study	N/A
pCAGGS _mC5aR1^{N283D}	This study	N/A
pCAGGS _C3aR	This study	N/A
pCAGGS_LgBiT-βarr1	Dr. Asuka Inoue	N/A
pCAGGS_LgBiT-βarr2	Dr. Asuka Inoue	N/A
pCAGGS_SmBiT-βarr1	Dr. Asuka Inoue	N/A
pCAGGS_SmBiT-βarr2	Dr. Asuka Inoue	N/A
pCAGGS_LgBiT-FYVE	Dr. Asuka Inoue	N/A

(*Continued on next page*)

Continued

REAGENT or RESOURCE	SOURCE	IDENTIFIER
pVL1393-FLAG-humanC5aR1	GenScript	N/A
pVL1393-FLAG-mouseC5aR1	GenScript	N/A
pVL1393-FLAG-C3aR	GenScript	N/A
pVL1392Dual-β1γ2 vector	GenScript	N/A
Software and algorithms		
Relion3.1.2	Zivanov et al.[61,62,63]	https://www3.mrc-lmb.cam.ac.uk/relion/index.php?title=Main_Page
cryoSPARC	Punjani et al.[64]	https://cryosparc.com/
UCSF Chimera X	Pettersen et al.[65]	https://www.rbvi.ucsf.edu/chimerax/
UCSF Chimera	Pettersen et al.[66]	https://www.cgl.ucsf.edu/chimera/
COOT	Casañal et al.[67]; Emsley et al.[68]; Emsley and Cowtan[69]	https://www2.mrc-lmb.cam.ac.uk/personal/pemsley/coot/
Phenix	Liebschner et al.[70]; Adams et al.[71]	https://www.phenix-online.org/
PDBePISA webserver	Krissinel and Henrick[72]	https://www.ebi.ac.uk/pdbe/pisa/
PDBsum	Laskowski et al.[73]	http://www.ebi.ac.uk/thornton-srv/databases/pdbsum/
Graphpad Prism v8 and v9	GraphPad Software, San Diego, California USA	https://www.graphpad.com/scientific-software/prism/
Others		
100kDa Cutoff Concentrators	Cytiva	Code# 28932319
30kDa Cutoff Concentrators	Cytiva	Code# 28932317
10kDa Cutoff Concentrators	Cytiva	Code# 28932296

RESOURCE AVAILABILITY

Lead contact

Further information and requests for reagents should be addressed to the lead contact Dr. Arun K. Shukla (arshukla@iitk.ac.in).

Materials availability

ALL unique reagents described in this manuscript are available from the lead contact with a completed Materials Transfer Agreement.

Data and code availability

- All three-dimensional cryo-EM density maps, coordinates for the atomic models and local-refined maps generated in this study have been deposited and are publicly available as of the date of publication. Accession numbers (EMDB and PDB IDs) are listed in the key resources table. Original gel images have been deposited to Mendeley data, and they are publicly available after publication. The DOI is listed in the key resources table.
- This paper does not report any original code.
- Any additional information required to reanalyze the data reported in this paper is available from the lead contact upon request.

EXPERIMENTAL MODEL AND STUDY PARTICIPANT DETAILS

Human cell line

HEK-293 cells were purchased from ATCC for all the cellular experiments performed in the study. The cell line was examined frequently under the microscope for proper morphology, but they were not authenticated or tested for mycoplasma contamination. They were cultured in DMEM with fetal bovine serum (FBS) at 37°C in 5% CO_2. In this study, any stable, knockout, or knockdown cell lines were not generated, and the details of previously generated cell lines are referenced in the manuscript.

Human monocyte cell-derived macrophages (HMDMs)

Human buffy coat blood from anonymous healthy donors was obtained through the Australian Red Cross LifeBlood Service (Brisbane, Australia) with the experimental approval by The University of Queensland Human Research Ethics Committee (approval reference 2020000559), and monocytes were isolated as mentioned in the subsequent method section. The isolated monocytes

were differentiated in Iscove's Modified Dulbecco's Medium supplemented with 10% FBS, 100 U mL^{-1} penicillin, 100 μg mL^{-1} streptomycin and 15 ng mL^{-1} recombinant human macrophage colony stimulating factor. Further demographic information on donors was not available as per the deed agreement with Australian Red Cross Lifeblood.

Insect cell line

Sf9 cells were obtained from Expression systems, and they were routinely monitored under the microscope for proper morphology, but they were not authenticated or tested for mycoplasma contamination. These cells were maintained in a shaker incubator at 27°C with 135rpm shaking, and sub-cultured in protein-free insect cell medium purchased from Expression Systems.

Bacterial cell culture

Escherichia coli strain DH5alpha were used for plasmid DNA amplification and isolation, and they were cultured in Luria-Bertani (LB) broth at 37°C with shaking at 160rpm. For protein expression, BL21 (DE3), Rosetta (DE3), SHuffle strains of *Escherichia coli* were used, and they were cultured using Luria-Bertani (LB), Terrific Broth (TB), or 2XYT media under the indicated culture conditions (temperature and shaking) as described in the subsequent method sections.

METHOD DETAILS

General chemicals, plasmids, and cell culture

Unless otherwise stated, most standard reagents were purchased from Sigma Aldrich. Dulbecco's Modified Eagle's Medium (DMEM), Phosphate Buffer Saline (PBS), Trypsin-EDTA, Foetal-Bovine Serum (FBS), Hank's Balanced Salt Solution (HBSS), and Penicillin-Streptomycin solution were purchased from Thermo Fisher Scientific. HEK-293T cells (ATCC) were maintained in DMEM (Gibco, Cat. no: 12800-017) supplemented with 10% (v/v) FBS (Gibco, Cat. no: 10270-106) and 100 U mL^{-1} penicillin and 100 μg mL^{-1} streptomycin (Gibco, Cat. no: 15140122) at 37 °C under 5% CO_2. *Sf9* cells were maintained in protein-free cell culture media purchased from Expression Systems (Cat. no: 96-001-01) at 27 °C with 135 rpm shaking. The cDNA coding region of C3aR was cloned in pcDNA3.1 vector with an N-terminal FLAG tag and in pVL1393 vector with an N-terminal FLAG tag followed by the N-terminal region of M4 receptor (residues 2-23). For the constructs used in NanoBiT assay to monitor C3aR/C5aR1-βarr interaction, SmBiT was fused at the C-terminus of the receptors and LgBiT was fused at the N-terminus of βarrs through sub-cloning. For endosomal localization assay, SmBiT was fused at the N-terminus of βarrs and LgBiT was fused at the N-terminus of the FYVE domain of the human Endofin protein. Additional technical details, assay establishment and optimization using these constructs have been described previously.[74,75] All DNA constructs were verified by sequencing from Macrogen. EP54, EP67, EP141 and $C5a^{pep}$ were synthesized from GenScript.

GloSensor-based cAMP assay

G-protein activation on agonist stimulation was quantified by GloSensor assay using cAMP level as readout as described previously.[76–78] Briefly, HEK-293 cells were co-transfected either with 5 μg of FLAG-tagged C3aR along with 2 μg F22 plasmid or 3.5 μg of FLAG-tagged C5aR1 along with 3.5 μg of F22 plasmid. Post 16-18 h of transfection, cells were trypsinized and harvested, followed by resuspension in assay buffer composed of 1X HBSS, 20 mM of 4-(2-hydroxyethyl)-1-piperazineethanesulfonic acid (HEPES), pH 7.4, and D-luciferin (0.5 mg mL^{-1}) (GoldBio, Cat. no: LUCNA-1G). Cells were seeded in 96-well flat bottom white plate (Corning) at a density of 200,000 cells per 100 μL and incubated at 37 °C for 90 min followed by 30 min incubation at room temperature. Basal readings were taken before ligand stimulation. To study ligand-induced Gi activation, cells were treated with forskolin at 1 μM concentration before stimulation, and readings were recorded until maximum luminescence signal was obtained. For stimulation, ligand concentrations were prepared by serial dilution in 1X HBSS, 20 mM HEPES, pH 7.4. The cells were stimulated with indicated doses of respective ligands. Changes in luminescence were recorded using a microplate reader (BMG Labtech). Data were normalized by treating the minimum agonist concentration as 100% and plotted using nonlinear regression analysis in GraphPad Prism software.

Surface expression assay

To study receptor surface expression, whole cell-based receptor surface ELISA was performed as previously discussed.[79] Briefly, cells transfected with receptor construct for respective assays were seeded in a 24-well with 0.01% poly-D-Lysine pre-coated plate at a density of 0.2 million cells $well^{-1}$ and incubated at 37°C for 24 h. After 24 h, the plate was removed, growth media was aspirated, and the plate was washed with ice-cold 1X TBS, followed by 20 min of fixation with 4% PFA (w/v in 1X TBS) on ice. After fixation, cells were washed thrice with 1X TBS (400 μL in each wash), followed by blocking with 1% BSA prepared in 1X TBS at room temperature for 90 min. Afterward, cells were incubated for 90 min with anti-FLAG M2-HRP (prepared in 1% BSA, 1:5000) (Sigma, Cat. no: A8592). Following antibody incubation, cells were washed thrice with 1% BSA (in 1X TBS). Thereafter, assay was developed by incubating cells with 200 μL of TMB-ELISA (Thermo Scientific, Cat no: 34028) until the light blue color appeared, followed by quenching with 100 μL of 1 M H_2SO_4 by transferring the blue-colored solution to a 96-well plate. Absorbance was measured at 450 nm using a multi-mode plate reader. Afterward, cells were washed twice with 200 μL of 1X TBS and then incubated with 0.2% Janus Green (Sigma; Cat no: 201677) w/v for 15 min. The excess stain was removed by three washes with distilled water. The stain was eluted

by adding 800 μL of 0.5 N HCl per well. 200 μL of the eluted solution was transferred to a 96-well plate, and absorbance was recorded at 595 nm. The signal intensity was normalized by calculating the ratio of A450/A595 values. For data normalization, the ratio of A450/A595 values was calculated, followed by considering pcDNA transfected cells reading as 1, and receptor expression was calculated with respect to pcDNA. Data were analyzed in GraphPad Prism software.

NanoBiT-based βarr-recruitment assay

Agonist-induced βarr1/2 recruitment to the plasma membrane downstream of C3aR and C5aR1 was measured by luminescence-based enzyme-linked complementation assay (NanoBiT-based assay) following the protocol described earlier.[80,81] Briefly, HEK-293 cells were transfected with C3aR (5 μg) and C5aR1 (1 μg of either mC5aR1 or hC5aR1) harboring carboxyl-terminus fusion of SmBiT and βarr1/2 constructs (2 μg for C3aR and 3.5 μg for C5aR1) with N-terminal fusion of LgBiT using transfection reagent polyethyleneimine (PEI) at DNA:PEI ratio of 1:3. Post 16-18 h of transfection, cells were trypsinized, harvested, and resuspended in the NanoBiT assay buffer (HBSS containing 0.01% BSA, 5 mM HEPES, pH 7.4, and 10 μM coelenterazine (GoldBio, Cat no: CZ05). After resuspension, 0.1 million cells per 100 μL were seeded in the flat-bottom white 96-well plate. The plate was incubated at 37 °C for 90 min, followed by 30 min at room temperature. After 2 h of incubation, three cycles of luminescence reading were taken before ligand addition in a multi-mode plate reader (BMG Labtech). Ligand concentrations were prepared by serial dilution in 1X HBSS, 20 mM HEPES, pH 7.4. The cells were stimulated with indicated doses of respective ligands followed by measurement of luminescence signal using a multi-mode plate reader for 20 cycles, and average data of 5 cycles showing highest range of luminescence were used for analysis and presentation. For measuring βarr1/2 recruitment to mC5aR1 mutants, following amount of DNA was used for each of the FLAG-tagged receptors harbouring carboxyl-terminus fusion of SmBiT: 1 μg for hC5aR1/mC5aR1, 2.5 μg for $mC5aR1^{E176V}$/ $mC5aR1^{Y178R}$ and 3.5 μg for $mC5aR1^{N283D}$/ $mC5aR1^{E280K}$ along with 3.5 μg of either βarr1/2 harbouring N-terminal fusion of LgBiT.

Agonist-induced endosomal trafficking of βarrs

Agonist-induced βarr1/2 trafficking to the endosomes was monitored using NanoBiT assay following the same protocol as described above for βarr recruitment. HEK-293 cells were transfected with βarr1/2 tagged with SmBiT at the N-terminus, and N-terminal LgBiT-tagged FYVE constructs were used for enzyme complementation. The amount of DNA for receptor, βarr1/2 and FYVE was kept at 1 μg (for hC5aR1 and mC5aR1) or 5 μg (for C3aR), 2 μg, and 5 μg, respectively.

Assays with HMDMs

HMDMs were generated and cultured as previously described,[33,82] with experiments approved by The University of Queensland Human Research Ethics Committee. Briefly, human buffy coat blood from anonymous healthy donors was obtained through the Australian Red Cross LifeBlood Service (Brisbane, Australia). Monocytes were isolated using Lymphoprep density centrifugation (STEMCELL, Melbourne, Australia) followed by $CD14^+$ MACS magnetic bead separation (Miltenyi Biotec, Sydney, Australia). The isolated monocytes were differentiated for 7 days in Iscove's Modified Dulbecco's Medium supplemented with 10% FBS, 100 U mL^{-1} penicillin, 100 μg mL^{-1} streptomycin (Thermo Fisher Scientific, Melbourne, Australia) and 15 ng mL^{-1} recombinant human macrophage colony stimulating factor (BioLegend, San Diego, USA) on 10 mm square dishes (Bio-strategy, Brisbane, Australia). Non-adherent cells were removed by washing with DPBS, and the adherent differentiated HMDMs were harvested by gentle scraping.

The immunomodulatory effect of human C3a (Merck) and EP141 on lipopolysaccharide (LPS)-induced cytokine release was assessed in HMDMs as previously described.[13,28] HMDMs were seeded in 96-well tissue culture plates (100,000 /well) for 24 h before treatment. All ligands were prepared in serum-free IMDM containing 0.1% BSA. For stimulation, cells were co-treated with 10 ng mL^{-1} LPS and C3a (10 nM) or EP141 (100 nM) for 24 h (37°C, 5% CO_2). The supernatant was collected and stored at -20°C till further use. The IL-6 and TNF-α levels in the supernatant were quantified using respective human enzyme-linked immunosorbent assay (ELISA) kits (BD OptEIA) as per the manufacturer's protocol.

Ligand-induced intracellular calcium mobilization was assessed using Fluo-4 NW Calcium Assay kit following the manufacturer's instructions (Thermo Fisher Scientific, Melbourne, Australia). Briefly, HMDMs were seeded (70,000/well) in black clear-bottom 96-well tissue culture plates overnight. Cells were firstly stained with the Fluo-4 dye in assay buffer (1X HBSS, 20 mM HEPES) for 45 min (37°C, 5% CO_2). C3a and EP141 dilutions were prepared in assay buffer containing 0.1% BSA. On a Flexstation 3 platform, the fluorescence (Ex/Em: 494/516 nm) was continually monitored for a total of 100 s with ligand addition performed at 16 s.

The ligand-induced phospho-ERK1/2 signaling was assessed using the AlphaLISA Surefire Ultra p-ERK1/2 (Thr202/Tyr204) kit (PerkinElmer, Melbourne, Australia) as previously described.[33,82] Briefly, HMDMs were seeded (50,000/well) in tissue culture-treated 96-well plates for 24 h and serum-starved overnight. C3a and EP141 serial dilutions were prepared in serum-free IMDM containing 0.1% BSA. For stimulation, cells were incubated with C3a or EP141 for 10 min at room temperature and then immediately lysed using AlphaLISA lysis buffer on a microplate shaker (450 rpm, 10 min). For the detection of phospho-ERK1/2 content, cell lysate (5 μL/well) was transferred to a 384-well ProxiPlate (PerkinElmer) and added to the donor and acceptor reaction mixes (2.5 μL/ well, respectively) with 2-h incubation at room temperature in the dark. The plate was read on Tecan Spark 20M following standard AlphaLISA settings.

Expression and purification of C3a and C3aR

Gene encoding human C3a was cloned in pET-32a(+) vector with a Trx-6X-His tag at the N-terminal end and purified following the previously described protocol for C5a purification with some modifications.[24,25] Briefly, freshly transformed *E. coli* SHuffle cells were inoculated in 50 mL 2XYT media with 100 μg mL^{-1}ampicillin for starter culture at 30°C. Overnight grown primary culture was inoculated into 1.5 L 2XYT media with 100 μg mL^{-1} ampicillin, and the culture was allowed to grow at 30°C. At O.D ~ 0.6, culture was induced with 1 mM IPTG and shifted to 16 °C for overnight induction. Cells were harvested and incubated with 1 mg mL^{-1} lysozyme in 50 mM HEPES, pH 7.4, 300 mM NaCl, 20 mM Imidazole, 1 mM PMSF, and 2 mM Benzamidine for 2 h at 4°C. Cells were disrupted with ultrasonication, and cell debris was removed with high-speed centrifugation. C3a was enriched on Ni-NTA resins using gravity flow. Nonspecific proteins were removed with extensive washing (50 mM HEPES, pH 7.4, 1 M NaCl, 20 mM Imidazole), and fusion-C3a was eluted with 50 mM HEPES, pH 7.4, 150 mM NaCl, 300 mM Imidazole. Trx-his tag was cleaved with 8-10 h TEV treatment (1:20 w/w, TEV: Fusion protein) at room temperature. Purified C3a was further cleaned by cation-exchange chromatography and stored at -80°C with 10% final glycerol concentration.

Codon-optimized human C3aR was expressed in *Spodoptera frugiperda* (*Sf9*) cells using the baculovirus expression system with an N-terminal FLAG tag to facilitate purification. The receptor was purified as described previously. Briefly, the insect cells were harvested at 72 h post-infection and lysed by sequential douncing in a low-salt buffer (20 mM HEPES, pH 7.4, 10 mM $MgCl_2$, 20 mM KCl, 1 mM PMSF, and 2 mM Benzamidine), high salt buffer (20 mM HEPES, pH 7.4, 1 M NaCl, 10 mM $MgCl_2$, 20 mM KCl, 1 mM PMSF, and 2 mM Benzamidine), and lysis buffer (20 mM HEPES, pH 7.4, 450 mM NaCl, 2 mM $CaCl_2$, 1 mM PMSF, 2 mM Benzamidine and 2 mM Iodoacetamide). After lysis, the receptor was solubilized for 2 h at 4°C with continual stirring in a solution of 0.5% L-MNG (Anatrace, Cat. no: NG310) and 0.1% cholesteryl hemisuccinate (Sigma, Cat. no: C6512). Post solubilization, salt concentration was lowered to 150 mM, and the receptor was purified on M1-FLAG column. In order to remove nonspecific proteins from FLAG beads, three washes of low salt buffer (20 mM HEPES, pH 7.4, 2 mM $CaCl_2$, 0.01% CHS, 0.01% L-MNG) were alternated with two washes of high salt buffer (20 mM HEPES, pH 7.4, 450 mM NaCl, 2 mM $CaCl_2$, 0.01% L-MNG) after binding. The bound receptor was eluted with FLAG elution buffer (20 mM HEPES, pH 7.4, 150 mM NaCl, 0.01% MNG, 2 mM EDTA, and 250 μg mL^{-1} FLAG peptide) and alkylated with iodoacetamide to prevent aggregation. The purified receptor was concentrated using a 30 kDa MWCO concentrator and stored at -80°C in 10% glycerol till further use. 100 nM of hC3a or 1 μM of EP54 and EP141 were kept in all steps of receptor purification.

Expression and purification of C5a, C5a$^{des\text{-}Arg}$, and C5aR1

Genes encoding human C5a and C5a$^{des\text{-}Arg}$ were cloned in pET-32a (+) vector with a Trx-6X-His tag at the N-terminal end and purified following previously described protocol with slight modification.[25,40] After Ni-NTA purification, we directly proceeded to TEV cleavage followed by cation-exchange chromatography. Codon-optimized human and mouse C5aR1 (hC5aR1 and mC5aR1) were expressed in *Spodoptera frugiperda* (*Sf9*) cells using baculovirus expression system with an N-terminal FLAG tag to facilitate purification. The receptor was purified as described previously.[13] Briefly, 72h post-infection, insect cells were harvested and lysed by sequentially douncing in low salt buffer (20mM HEPES pH 7.4, 10mM $MgCl_2$, 20mM KCl, 1mM PMSF, and 2mM Benzamidine), high salt buffer (20mM HEPES pH 7.4, 1M NaCl, 10mM $MgCl_2$, 20mM KCl, 1mM PMSF, and 2mM Benzamidine), and lysis buffer (20mM HEPES pH 7.4, 450mM NaCl, 2mM $CaCl_2$, 1mM PMSF, 2mM Benzamidine and 2mM Iodoacetamide). After lysis, receptor was solubilized in 0.5% L-MNG (Anatrace, Cat. no: NG310) and 0.1% cholesteryl hemisuccinate (Sigma, Cat. no: C6512) for 2 h at 4°C, under constant stirring. Post-solubilization, salt concentration was lowered to 150mM, and the receptor was purified on M1-FLAG column. After binding, FLAG beads were washed alternately with three washes of low salt buffer (20mM HEPES pH 7.4, 2mM $CaCl_2$, 0.01% CHS, 0.01% L-MNG) and two washes of high salt buffer (20mM HEPES pH 7.4, 450mM NaCl, 2mM $CaCl_2$, 0.01% L-MNG) to remove non-specific proteins. The bound receptor was eluted with FLAG elution buffer (20mM HEPES pH 7.4, 150mM NaCl, 0.01% MNG, 2mM EDTA, and 250μg mL^{-1} FLAG peptide) and alkylated with iodoacetamide to prevent aggregation. The purified receptor was concentrated using a 30kDa MWCO concentrator and stored at -80°C in 10% glycerol till further use. 100 nM of C5a and C5a$^{des\text{-}Arg}$, or 1μM of C5a^{pep} were kept in all steps of receptor purification.

Expression and purification of G proteins

Construct for miniGαo and miniGαq were synthesized as described previously[83,84] with additional ScFv16 binding sequence at N-terminus of miniGαo. Briefly Genes for miniGαo1 and miniGαq subunit were cloned in pET-15b (+) vector with an in-frame 6X-His tag at the N-terminal and expressed in *E. coli* BL21(DE3) cells.[83,84] A starter culture in LB media was grown at 37°C for 6-8 h at 220 rpm. This was followed by an overnight primary culture at 30°C with 0.2% glucose supplementation.15 mL primary culture was inoculated in 1.5 L TB (Terrific Broth) media and induced with 50 μM IPTG at an O.D of 0.8 and cultured at 25°C for 18-20 h. Cells were lysed in lysis buffer (40 mM HEPES, pH 7.4, 100 mM NaCl, 10 mM Imidazole, 10% Glycerol, 5 mM $MgCl_2$, 1 mM PMSF, 2 mM Benzamidine) in the presence of 1 mg mL^{-1} lysozyme, 50 μM GDP and 100 μM DTT. Cell debris was pelleted down by centrifuging at 18000 rpm for 30 min at 4°C. Protein was enriched on Ni-NTA bead and after washing extensively with wash buffer (20 mM HEPES, pH 7.4, 500 mM NaCl, 40 mM Imidazole, 10% Glycerol, 50 μM GDP and 1 mM $MgCl_2$), eluted with elution buffer (20 mM HEPES, pH 7.4, 100 mM NaCl, 10% Glycerol, 500 mM Imidazole). His tag was cleaved by overnight TEV treatment at room temperature (1:20, TEV: protein), and untagged protein was recovered by size exclusion chromatography on Hi-Load Superdex 200 PG 16/600 column (Cytiva, Cat. no. 17517501). Fractions corresponding to cleaved protein were pooled, analyzed on SDS-PAGE, and stored at -80°C with 10% glycerol. The genes encoding the Gβ1 and Gγ2 subunits cloned in a bi-cistronic pVL1932-

based vector with N-terminal histidine tag at the Gβ1 were expressed in *Sf9* cells using the baculovirus expression system. Cells were harvested 72 h after infection and resuspended in lysis buffer (20 mM Tris-Cl, pH 8.0, 150 mM NaCl, 10% Glycerol, 1 mM PMSF, 2 mM Benzamidine and 1 mM $MgCl_2$). The cells were lysed via douncing and centrifuged at 4°C for 40 min at 18000 rpm. Pellet was resuspended and dounced in solubilization buffer (20 mM Tris-Cl, pH 8.0, 150 mM NaCl, 10% Glycerol, 1% DDM, 5 mM β-ME, 10 mM Imidazole, 1 mM PMSF, and 2 mM Benzamidine) and solubilized at 4°C under constant stirring for 2 h. Cell debris was pelleted down by centrifuging at 20000 rpm for 40 min at 4°C. Protein was enriched on Ni-NTA resin, and after extensive washing with wash buffer (20 mM Tris-Cl, pH 8.0, 150 mM NaCl, 30 mM Imidazole, 0.02% DDM), the protein was eluted with 300 mM Imidazole in 20 mM Tris-Cl, pH 8.0, 150 mM NaCl, 0.01% MNG. Eluted protein was concentrated with a 10 kDa MWCO concentrator (Cytiva Cat no: GE28-9322-96) and stored at -80°C with 10% glycerol.

Expression and purification of ScFv16

Gene encoding ScFv16 was cloned in pET-42a (+) vector with an in-frame N-terminal 10X-His-MBP tag followed by a TEV cleavage site and expressed in *E. coli* Rosetta (DE3) strain.[85] Overnight primary culture was sub-cultured in 1L 2x YT media supplemented with 0.5% glucose and 5 mM $MgSO_4$. At $O.D_{600}$ ~0.6, culture was induced with 250 μM IPTG for 16–18 h at 18°C. Cells were resuspended in 20 mM HEPES, pH 7.4, 200 mM NaCl, 2 mM Benzamidine, and 1 mM PMSF and incubated at 4°C for 1 h with constant stirring. Cells were disrupted by ultrasonication, and cell debris was removed by centrifugation at 18000 rpm for 40 min at 4°C. Protein was enriched on Ni-NTA resins, and non-specifically bound proteins were removed by extensive washing (20 mM HEPES, pH 7.4, 200 mM NaCl, 50 mM Imidazole). Bound protein was eluted with 300 mM Imidazole in 20 mM HEPES, pH 7.4, 200 mM NaCl. Subsequently, Ni-NTA elute was enriched on amylose resin (NEB, Cat. no: E8021L) and washed with buffer (20 mM HEPES pH 7.4, 200 mM NaCl) to remove nonspecific proteins. Protein was eluted with 10 mM maltose (prepared in 20 mM HEPES, pH 7.4, 200 mM NaCl), and the His-MBP tag was removed by overnight treatment with TEV protease. Tag-free ScFv16 was recovered by passing TEV-cleaved protein through Ni-NTA resin. Eluted protein was concentrated and cleaned by size exclusion chromatography on Hi-Load Superdex 200 PG 16/600 column (Cytiva Life sciences, Cat. no: 17517501). Purified protein was flash-frozen and stored at -80°C with 10% glycerol.

Reconstitution of the C3a/EP54/EP141-C3aR-Gαo/Gαq-Gβγ-ScFv16 complexes

Purified C3aR was incubated with 1.2 molar excess of Gαo, Gβ1γ2, and ScFv16 at room temperature for 2 h in the presence of 25 mU mL^{-1} apyrase (NEB, Cat. no: M0398S) and either C3a or EP54 or EP141 for complex formation. The G-protein complex was separated from unbound components by loading on Superose 6 increase 10/300 GL SEC column and analyzed by SDS PAGE. Complex fractions were pooled and concentrated to ~10 mg mL^{-1} using a 100 MWCO concentrator (Cytiva, Cat. no: GE28-9323-19) and stored at -80°C until further use.

Reconstitution of the C5a/C5a^{pep}-C5aR1-Gαoβ1γ2-ScFv16 complexes

Purified m/hC5aR1 was incubated with 1.2 molar excess of Gαo, Gβ1γ2, and ScFv16 at room temperature for 2 h in the presence of 25 mU mL^{-1} apyrase (NEB, Cat. no: M0398L) and either C5a/C5a^{pep}/C5a$^{des\text{-}Arg}$ for complex formation. The G-protein complex was separated from unbound components by loading on Superose 6 increase 10/300 GL SEC column and analyzed on SDS PAGE. Complex fractions were pooled and concentrated to ~10mg mL^{-1} using a 100MWCO concentrator (Cytiva, Cat. no: GE28-9323-19) and stored at -80°C until further use.

Single-particle, negative-stain electron microscopy

In order to confirm homogeneity and complex formation, negative stain electron microscopy was performed on all the samples before proceeding on with grid preparation for cryo-EM data collection. The individual samples were diluted to 0.02 mg mL^{-1} just prior to grid preparation and 3 μL of the samples were dispensed onto the carbon side of a glow discharged carbon/formvar coated 300 mesh Cu grids (PELCO, Ted Pella). The extra protein sample was blotted off after incubation for 1 min using a filter paper. The grid with the adsorbed protein sample was then touched on a first drop of 0.75% uranyl formate stain, and immediately blotted off using a filter paper. The grid was then touched onto a second drop of stain and moved gently in a rotating fashion for 30 s to increase the efficiency of staining. The grid so prepared was then left in a desiccator or on the bench in a petri-plate for air drying. Data collection was performed with a FEI Tecnai G2 12 Twin TEM (LaB6) operating at 120 kV and equipped with a Gatan CCD camera (4k x 4k) at 30,000x magnification. Processing of the collected dataset was performed with Relion 3.1.2[61–63] where almost 10,000 particles were autopicked and subjected to reference free 2D classification, generating the 2D class averages.

Cryo-EM grid preparation and data collection

Purified ligand-C3aR-Go complexes were applied onto glow-charged grids (EasiGlow, 20 mA current with 40 s glow and 10 s hold) at ~10 mg mL^{-1} concentration and blotted for 5-7 s followed by plunge-freezing into liquid ethane using a Vitrobot MarkIV (Thermo Fisher Scientific, USA) operating at 100% humidity. Briefly, ligand free-C3aR-Go and EP54-C3aR-Go complexes were applied onto Quantifoil R1.2/1.3 Au 300-mesh grids and blotted for 5 s at 4°C. For C3a-C3aR-Go, EP54-C3aR-Gq, C5a-hC5aR1-Go, EP141-C3aR-Go, and C5a$^{des\text{-}Arg}$-hC5aR1-Go complexes, the sample was applied onto Quantifoil R1.2/1.3 Au 200-mesh grids and blotted for 5-7 s at either 4 or 22°C. Cryo-EM data were collected using a Glacios microscope operating at 200 kV with a Falcon

4 direct electron detector operating in counting mode at nominal magnification of 150,000x resulting in pixel size of 0.92 Å using EPU. An additional dataset of ligand free-C3aR-Go was collected using Titan Krios operating at 300 kV with a Gatan K3 direct electron detector operating in counting mode at 105,000 magnifications with a pixel size of 0.86 Å (2-fold binned) using SerialEM. Movies were recorded with a defocus range of -0.8 to -3.0 μm and total dose of ~50 e^-/A^2. Additional data collection parameters are listed in Figures S4, S5, S6, S7, and S8. Total 4,611 movies for ligand-free-C3aR-Go (Glacios), 5,740 for ligand free-C3aR-Go (Titan), 20,051 movies for C3a-C3aR-Go, 4,614 movies for EP54-C3aR-Go, 4,445 movies for EP54-C3aR-Gq, 10,151 movies for C5a-hC5aR1-Go, 9,276 movies for $C5a^{des\text{-}Arg}$-hC5aR1-Go, and 15,216 movies for EP141-C3aR-Go were recorded.

For the cryo-EM data collection on mouse C5aR1 complexes, 3 μL of the purified complexes of C5a-mC5aR1-Go or $C5a^{pep}$-mC5aR1-Go were applied onto glow discharged Quantifoil holey carbon grids (Au, R2/1 M300) and vitrified using a Vitrobot Mark IV (Thermo Fisher Scientific, USA) operating at 10°C and maintained at 90% humidity. Data collection was performed with a Titan Krios electron microscope (Thermofisher Scientific, USA) operating at 300 kV equipped with Gatan Energy Filter. Movies were recorded in counting mode with a Gatan K2 Summit direct electron detector DED (Gatan, USA) using the automated SerialEM software at a nominal magnification of 165,000x and a pixel size of 0.82 Å at the specimen level. Total 22,014 movie stacks for C5a-mC5aR1-Go and 24,711 movie stacks for $C5a^{pep}$-mC5aR1-Go consisting of 40 frames were collected with a defocus value in the range of 0.5 to 2.5 μm with a total accumulated dose of 42 e^-/A^2 and total exposure time of 4 s.

Image processing and map construction

The overall cryo-EM data processing pipeline for all structures are shown in Figures S3 and S4. Data processing for EP54-C3aR-Go, C3a-C3aR-Go, Apo-C3aR-Go, EP54-C3aR-Gq, C5a-hC5aR1-Go and EP141-C3aR-Go complexes were performed in cryoSPARC version 4.0,[64] whereas that of $C5a^{pep}$-mC5aR1-Go and C5a-mC5aR1-Go were performed with cryoSPARC version 3.3.2.[64] Cryo-EM movie stacks were aligned using Patch motion correction (multi) followed by CTF estimation with Patch CTF estimation (multi). Micrographs were curated based on CTF resolution and selected micrographs were used for particle picking using blob-picker.

For the apo-C3aR-Go complex, two independent datasets were collected – one with Titan Krios microscope operating at 300 kV and the other with a Glacios microscope operating at 200 kV. For the Glacios dataset, 2D class averages with clear secondary features were selected to prepare a sub-set of 693,550 particles for further processing. Subsequent ab-initio reconstruction and 3D/Heterogeneous classification with C1 symmetry yielded the best class with 464,408 particles which was further refined to an overall resolution of 3.19 Å (voxel size of 1.063 Å) with NU refinement. For the apo-C3aR-Go Titan dataset, total 754,251 particles corresponding to 2D averages with clear secondary structural features were selected, re-extracted with a box size of 416 px and Fourier cropped to 256 px (pixel size 1.40 Å). This clean particle stack was used for multiclass ab-initio reconstruction followed by heterogeneous classification. Non-uniform refinement with 327,193 particles from the best 3D class yielded a map with a final estimated global resolution of 3.26 Å (voxel size of 1.40 Å).

For the C3a-C3aR-Go dataset, post-2D classification, 922,698 selected particles were extracted with a box size of 416 px and fourier cropped to 360 px (pixel size of 1.063 Å). This clean particle stack was then subjected to ab-initio reconstruction and heterogeneous refinement. The 3D class containing 418,953 particles with evident secondary features were subjected to non-uniform refinement, followed by local refinement with mask to exclude the micelle resulting in a final map at 3.18 Å resolution (voxel size of 1.063 Å). The density corresponding to C3a was noisy, therefore, local refinement was performed with a mask covering the C3a to improve the interpretability of the map in this region yielding a map with global resolution of 4.55 Å. The two local refinement maps were combined to obtain a composite map which was used for subsequent model building.

For the EP54-C3aR-Go complex dataset, a clean particle stack of 767,052 from the 2D classification step was selected and re-extracted with a box size of 360 px and fourier cropped to 256 px (pixel size of 1.495 Å). This particle stack was subjected to ab-initio reconstruction, followed by heterogenous refinement with C1 symmetry. Total 600,173 high-quality particles with evident structural features were selected and subjected to non-uniform refinement with C1 symmetry, followed by local refinement with a mask on the micelle. This led to a reconstruction with a global estimated resolution of 2.88 Å (voxel size of 0.92 Å). Local resolution estimation was performed with the Blocres sub-program within cryoSPARC version 4.0. Maps were sharpened using the "Autosharpen" sub-program within the Phenix suite[82] for better visualization and model building.

Initial processing of EP54-C3aR-Gq micrographs showed limited top/bottom views. Therefore, a conventional neural network-based method TOPAZ,[83] implemented in cryoSPARC, was used for particle picking. Briefly, Topaz was trained on 37,054 particles picked from denoised micrographs with the ResNet8 convolutional neural network model using down-sampling factor 8, and the expected number of particles per micrograph was set to 500. A total of 2,007,547 particles were picked, extracted, and subjected to iterative rounds of reference-free 2D classification followed by multiclass ab-initio reconstruction/heterogeneous refinement. The best 3D class with 101,400 particles was selected for subsequent non-uniform refinement, which yielded a map of 3.57 Å resolution.

For the C5a-hC5aR1-Go complex, 10,259,948 particle projections were selected and re-extracted with a box size of 416 px, fourier cropped to 256 px (pixel size of 1.50 Å). These extracted particles were used for generating 2 ab-initio models for subsequent heterogeneous refinement. The best class containing 292,441 particle projections were subjected to non-uniform refinement to obtain a density map with nominal resolution of 3.21 Å (voxel size of 1.06 Å). Density corresponding to C5a was poorly resolved, thus local refinement was done with a mask covering the C5a density to improve the interpretability of the map. The focused refinement against C5a yielded a map with final global resolution of 3.88 Å. The two maps were combined with "Combine focus maps" within Phenix to obtain a composite map which was used for model building.

For the C5a-mC5aR1-Go dataset, automated particle picking with blob-picker resulted in 2,601,754 particles which were extracted with a box size of 360 px and fourier cropped to box size of 64 (pixel size of 4.61). These particles were then subjected to several rounds of 2D classification and class averages with clear conformations of the complex were selected and extracted with a box size of 360 px and fourier cropped to 256 px (pixel size of 1.15). These clean set of particles were subjected to Ab-initio reconstruction and heterogeneous refinement yielding 3 models. A particle stack with 173,416 particles corresponding to the 3D class with evident secondary features were re-extracted with full box size of 416 px and fourier cropped to 360 px. This was followed by non-uniform refinement and local refinement with mask on the complex resulting in a final map at 3.89 Å resolution (voxel size of 0.9476 Å).

For C5a^{pep}-mC5aR1-Go complex, 1,886,363 particles were autopicked with the blob-picker sub-program within the cryoSPARC suite, extracted with a box size of 360 px and fourier cropped to 64 px (pixel size of 4.61) for reference free 2D classification. Several rounds of iterative 2D classification yielded class averages representing different orientations of the complex. A subset of 835,654 clean particles from the 2D classification were re-extracted with a box size of 360 px and fourier cropped to 256 px (pixel size of 1.15). This was followed by Ab-initio reconstruction and heterogenous refinement with C1 symmetry yielding 3 models. 380,463 particles corresponding to the class with clear complex conformation were re-extracted with full box size of 416 px, fourier cropped to 360 px and subjected to non-uniform refinement followed by local refinement with mask on the complex excluding the micelle yielding a reconstruction at 3.39 Å resolution (voxel size of 0.9476 Å).

For the C5a$^{des\text{-}Arg}$-hC5aR1-Go dataset, 8,932 motion corrected micrographs with CTF fit resolution better than 4 Å were selected for further processing. 8,059,635 particles were autopicked with the blob-picker subprogram, extracted with a box size of 360 px (fourier cropped to 64 px) and subjected to 2D classification. 1,013,163 particles corresponding to the clean 2D class averages were selected, re-extracted with a box size of 360 px (fourier cropped to 180 px) and subjected to ab-initio reconstruction and subsequent heterogeneous refinement yielding 3 classes. 860,786 particles corresponding to the best class with clear secondary features were re-extracted with full box size of 360 px and subjected to non-uniform refinement yielding a final reconstruction with an overall resolution of 3.31 Å at 0.143 cutoff.

For the EP141-C3aR-Go dataset, 15,216 motion corrected micrographs were manually curated and 12,114 micrographs with CTF fit resolution greater than 4 Å were selected for automated particle picking with the blob-picker subprogram. 9,530,582 autopicked particles were extracted with a box size of 416 px and fourier cropped to 64 px for subsequent reference free 2D classification. 2D classes with clear secondary features were selected and re-extracted with a box size of 360 px and fourier cropped to 288 px for generating 4 ab-initio reconstructions and downstream heterogenous refinement. 914,579 particles corresponding to the best 3D class with essential features of a GPCR-G protein complex were selected and subjected to non-uniform refinement to yield a map with an estimated resolution of 3.1 Å at 0.143 cutoff.

Model building and refinement

For the C5a^{pep}-mC5aR1-Go complex, the receptor coordinates from the cryo-EM structure of human formyl peptide receptor 2 (PDB: 7WVV)[58] and the coordinates for the Gαo, Gβ1, Gγ2 from the cryo-EM structure of Muscarinic acetylcholine receptor 2-Go complex (PDB: 6OIK)[59] were used as an initial model to dock into the EM density using Chimera.[65,66] This was followed by manual rebuilding of the model along with the ligand in COOT[67–69] and iterative real space refinement in Phenix.[70,71] This yielded a model with 96.63% in the most favored region and 3.37% in the allowed region of the Ramachandran plot.

For the C5a-mC5aR1-Go complex map, the coordinates of C5a^{pep}-mC5aR1-Go complex was used as an initial model and docked into the EM density with the "Fit in map" extension in Chimera. Similarly, the coordinates corresponding to human C5a were taken from a previously solved crystal structure of the human C5a in complex with MEDI7814, a neutralizing antibody (PDB: 4UU9).[60] The model so obtained was docked in Chimera, manually rebuilt in COOT and subjected to several rounds of real space refinement in Phenix to reach a final model with 95.87% in the favored region and 4.13% in the allowed region of the Ramachandran plot. Data collection, 3D reconstruction and refinement statistics have been included as Table S1.

Coordinates of C5aR1 receptor, Gαo, Gβ1 and Gγ2 from the cryo-EM structure of C5a-pep-C5aR1-Go (PDB: 8HPT) were used as initial models to dock into the EM density of EP54-C3aR-Go complex using the "Fit in map" extension in Chimera.[65,66] The fitted model along with the map was imported into COOT[67–69] for manual rebuilding of the model along with the ligand (EP54), with iterative rounds of real space refinement in Phenix.[70,71] This yielded a final refined model with 94.95% of the residues in the most favored region and 5.05% in the allowed region of the Ramachandran plot.

For the C3a-C3aR-Gαo complex map, coordinates of the receptor, Gαo, Gβ1 and Gγ2 from EP54-C5aR1-Gαo complex were used as initial models. The coordinates of C3a were obtained from a previously solved crystal structure of C3a (PDB: 4HW5).[24] Chimera was used to dock the individual components in the cryo-EM map and obtain a merged model. The combined model was manually rebuilt in COOT[61–63] and subjected to multiple rounds of real space refinement in Phenix. The final refined model showed good validation statistics with 95.44% in the favored region and 4.56% in the allowed region of the Ramachandran plot.

For EP54-C3aR-Gq and both the ligand free-C3aR-Go cryo-EM maps, the coordinates corresponding to the individual components were obtained from the model of EP54-C3aR-Go which were used to fit into the coulombic map with the "Fit in map" extension in Chimera. Iterative rounds of manual adjustment and building in COOT[67–69] and refinement with real space refine in Phenix resulted in the final model with excellent validation statistics and no Ramachandran outliers. For ligand free-C3aR-Go, the model obtained from the Glacios data was used for analysis of the ligand free structure due to its higher resolution and more interpretable map. Data collection and refinement statistics have been included in the supplemental information.

For the C5a-hC5aR1-Go complex map, the coordinates for the receptor were taken from the cryo-EM structure of human formyl peptide receptor 2 (PDB: 7WVV), while the coordinates for Gαo, Gβ1, Gɣ2 were obtained from the cryo-EM structure of $C5a^{pep}$-mC5aR1-Go complex. The coordinates were docked into the EM density map in Chimera and the combined model so obtained were transferred to COOT for performing subsequent mutations and model manipulations. Several rounds of real space refinement in Phenix yielded the final model with 92.90% in the favored region and 7.10% in the allowed region of the Ramachandran plot.

For the $C5a^{des\text{-}Arg}$-hC5aR1-Go complex, the atomic coordinates of C5a, C5aR1, Gαo, Gβ1 and Gɣ2 were obtained from the cryo-EM structure of C5a-hC5aR1-Go structure (PDB: 8IA2), and docked into the electron microscopy density map using UCSF Chimera, followed by iterative manual adjustment and rebuilding in COOT. The coordinates were refined against the final map using phenix.real_space_refine with secondary structure and geometry restraints. The final refined model showed excellent statistics with 95.59% in the most favored region and 4.41% in the allowed region of the Ramachandran plot.

For the EP141-C3aR-Go complex, the coordinates of C3aR, Gαo, Gβ1 and Gɣ2 were obtained from EP54-C5aR1-Go complex structure and were used as initial models to dock into the coulombic map using Chimera. The merged model obtained was imported into COOT and further fitted into the density with the ''Fit in map'' extension. The EP141 peptide ligand was then manually built into the ligand density followed by multiple rounds of real space refinement with phenix.real_space_refine. The final model so obtained exhibited good statistics with 96.19% in the most favored region and 3.81% in the allowed region of the Ramachandran plot.

All figures were prepared either with Chimera or ChimeraX software.[65,66] Buried surface and interface surface area have been calculated with PDBePISA webserver.[72] Ligand-receptor and receptor-G-protein interactions were identified using using PDBsum.[73]

QUANTIFICATION AND STATISTICAL ANALYSIS

GraphPad Prism v9.5 was used to plot and analyze all the functional data presented in this manuscript, and all the relevant details such as number of replicates, data normalization, mean ± SEM, and statistical analyses are mentioned in the corresponding figure legends.

CellPress
OPEN ACCESS

Supplemental figures

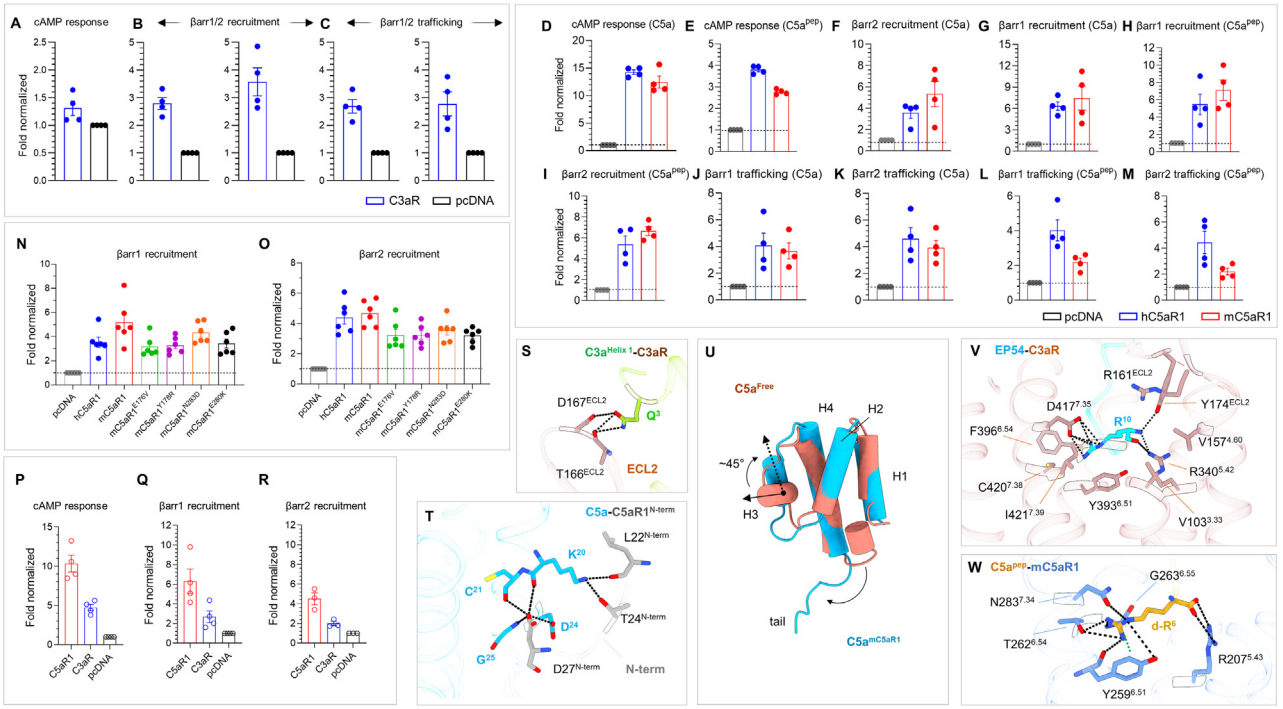

Figure S1. Surface expression profiles of C3aR and C5aR1 and critical interactions of C3a/C5a with C3aR/C5aR1, related to Figures 1, 3, and 7

(A) Surface expression of C3aR in GloSensor measured using whole-cell ELISA (mean ± SEM; n = 4; normalized as fold over mock transfection).

(B) Surface expression of C3aR in βarr1/2 recruitment assay (mean ± SEM; n = 4; normalized as fold over mock transfection).

(C) Surface expression of C3aR in βarr1/2 endosomal trafficking assay (mean ± SEM; n = 4; normalized as fold over mock transfection).

(D–M) Surface expression of indicated receptors measured using whole-cell ELISA (mean ± SEM; n = 4; normalized as fold over mock transfection) in various assays.

(N and O) Surface expression of indicated receptor constructs in βarr1 and βarr2 recruitment assays (mean ± SEM; n = 6, normalized as fold over mock transfection).

(P) Surface expression of C3aR and C5aR1 in GloSensor assay (mean ± SEM; n = 4; normalized as fold over mock transfection).

(Q and R) Surface expression of C3aR and C5aR1 in βarr1 (mean ± SEM; n = 4) and βarr2 (mean ± SEM; n = 4) recruitment assay (normalized as fold over mock transfection).

(S and T) Interface between Gln^3 of C3a with C3aR and C5a with N-term of C5aR1.

(U) Structural comparison of free C5a with C5a bound to mC5aR1. H3 of C5a can be seen to exhibit a rotation of ~45° upon binding to the receptor.

(V and W) The terminal arginine in EP54 and $C5a^{pep}$ makes extensive interactions with C3aR and C5aR1, respectively.

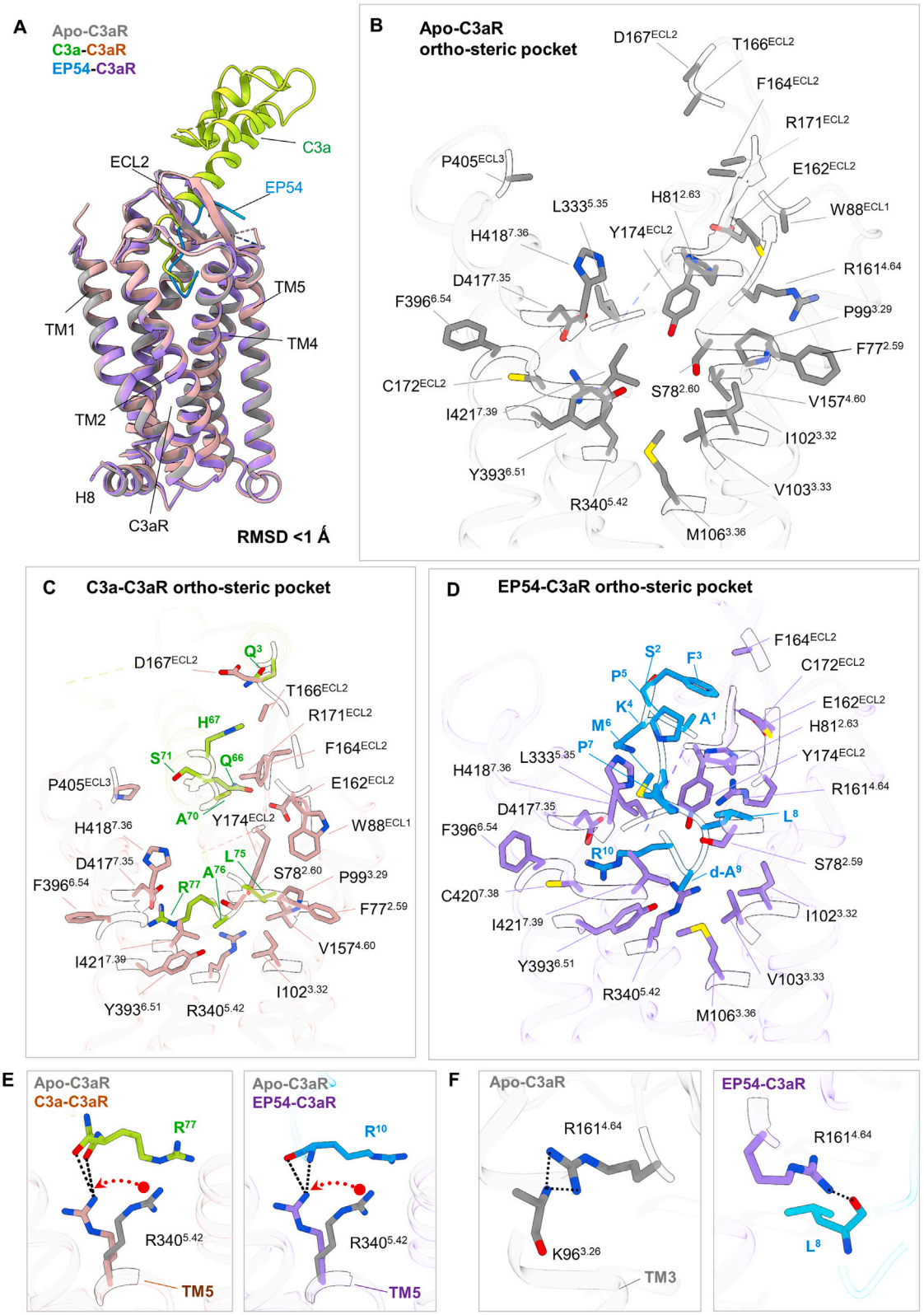

(legend on next page)

Figure S2. Comparison of the residues in the orthosteric pocket of C3aR in Apo-, EP54-, and C3a-bound states, related to Figure 3

(A) Structural superimposition of Apo-, EP54-, and C3a-bound C3aR-Go complexes.

(B) Conformation of all the residues present in the orthosteric pocket of C3aR involved in interaction with the ligands are shown in the Apo structure.

(C and D) Residues of the orthosteric pocket of C3aR involved in interaction with the residues of C3a (C) and EP54 (D) are highlighted.

(E and F) Changes in rotameric conformations of Arg340$^{5.42}$ and Arg161$^{4.64}$ in the Apo state as compared with the ligand-bound state.

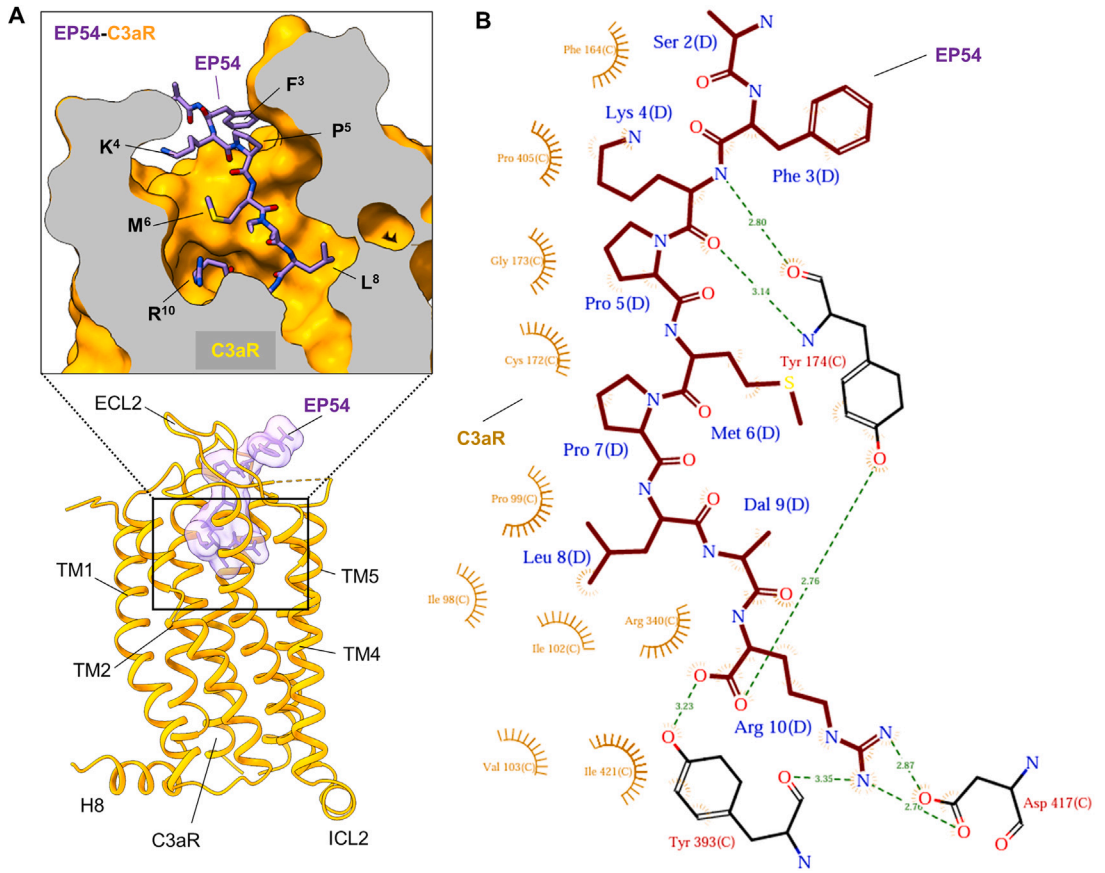

D

EP54-C3aR-Go		EP54-C3aR-Gq
Specific contacts	Common contacts	Specific contacts
F77	P99	I98
S78	I102	P405
H81	V103	
M106	R161	
V157	F164	
R171	C172	
L333	G173	
F396	Y174	
G397	R340	
C420	Y393	
	D417	
	I421	

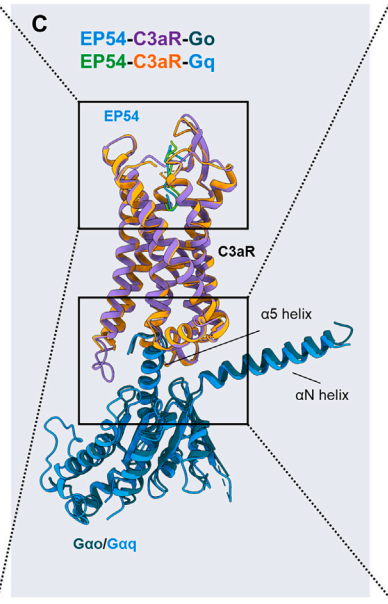

E

EP54-C3aR-Go		EP54-C3aR-Gq
Specific contacts	Common contacts	Specific contacts
D119	N57	R362
Y435	R120	R367
G439	V123	F368
	V124	S371
	P127	V378
	Q131	
	N132	
	N135	
	I359	
	K374	
	T375	

Figure S3. EP54 binding and activation of C3aR in complex with Gq and comparison with Go-bound state, related to Figures 3 and 6

(A) EP54 binding pose at the orthosteric pocket of C3aR in complex with Gq. EP54 in transparent surface (bottom) and receptor in surface slice showing side chains of EP54 in the ligand-binding pocket (top).

(B) Interaction interface between EP54 and C3aR-Gq. The interaction plot has been generated through PDBSum.

(C) Structural superposition of EP54-C5aR-Gαo and EP54-C3aR-$G\alpha_q$ complexes.

(D and E) Common and specific residue interactions between C3aR and EP54 (D) and C3aR and Gαo/Gαq (E), respectively.

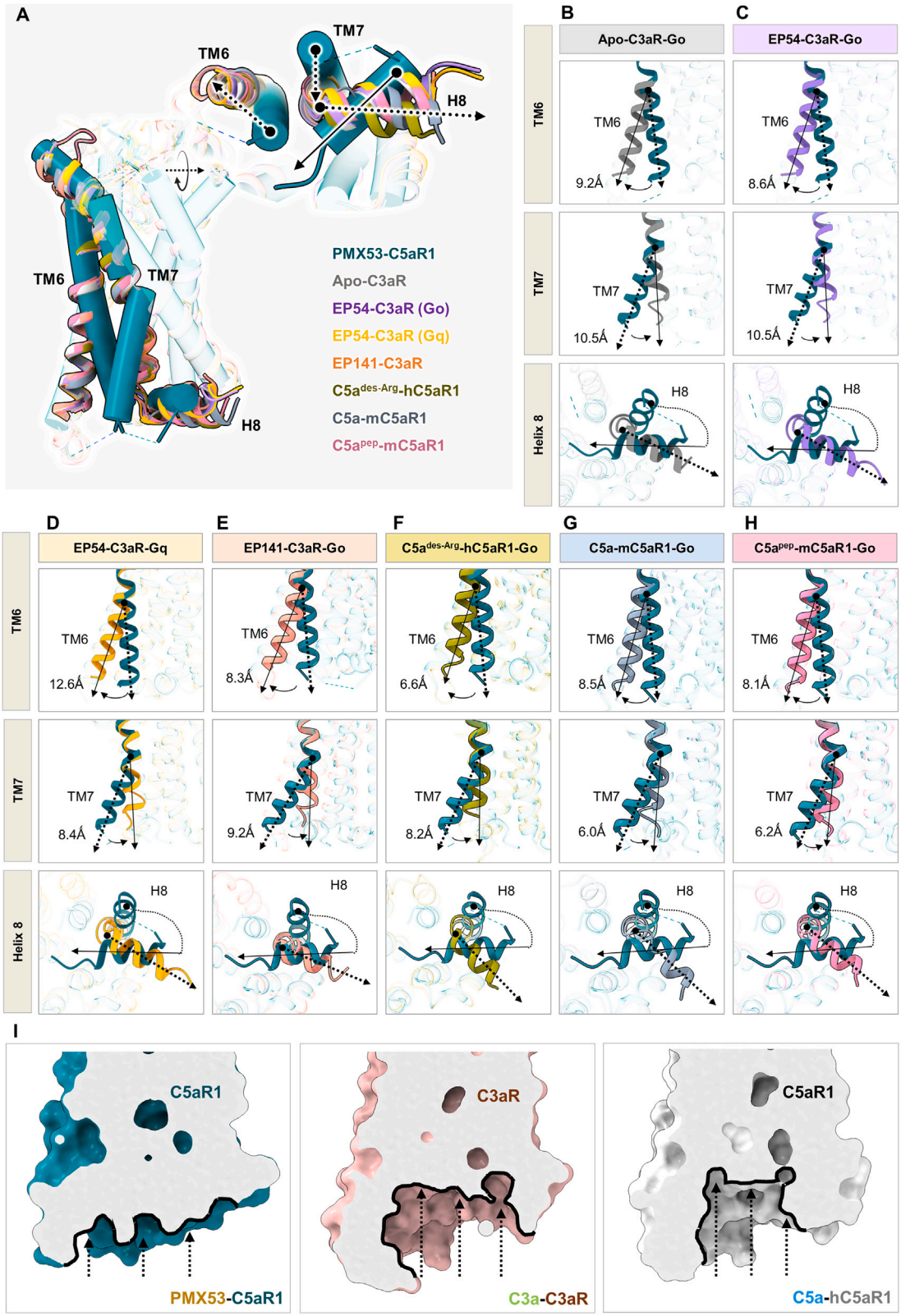

(legend on next page)

Figure S4. Active conformations of C3aR and C5aR1, related to Figure 6

(A) Structural superimposition of C3a-bound C3aR and C5a-bound hC5aR1 with inactive C5aR1 (PDB: 6C1R). TM6, TM7, and H8 are highlighted to show the change in conformation in the receptors, and other regions are depicted in transparent ribbons.

(B–H) Dynamic changes in TMs of activated C3aR/C5aR1 compared with the inactive state of C5aR1. The TMs and H8 from different receptor complexes shown are from receptors mentioned in boxes. Solid lines (active receptors) and dotted lines (inactive C5aR1) indicate direction of movement. The respective degrees of movements in corresponding TMs have also been mentioned.

(I) The antagonist PMX53 (PDB: 6C1R) occupies an analogous binding pocket on C5aR1 and adopts a hook-like conformation similar to C5a (left). However, the cytoplasmic cavity in the inactive-state structure C5aR1 is blocked thereby preventing further transducer coupling compared with the active state C3aR and C5aR1 (middle and right).

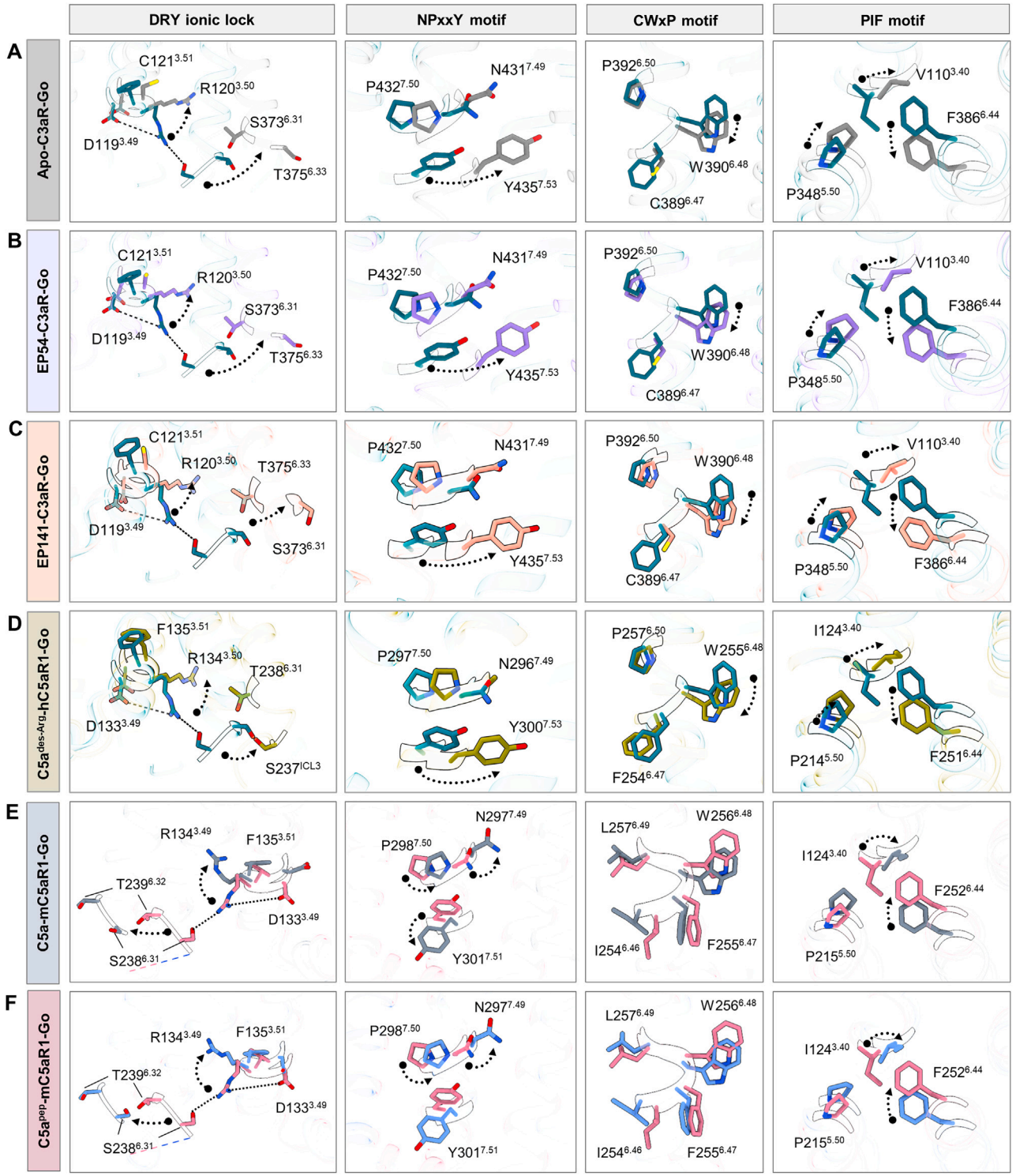

Figure S5. Conformational changes in the conserved microswitches of C3aR and C5aR1, related to Figure 6

(A–F) Conformational changes in the conserved microswitches: (DRY(F), NPxxY, C(F)WxP(L), and PIF) upon C3aR and C5aR1 activation. (Teal and pink: inactive C5aR1 for C3aR and C5aR1 structures, respectively, various colors: C3aR and C5aR1.)

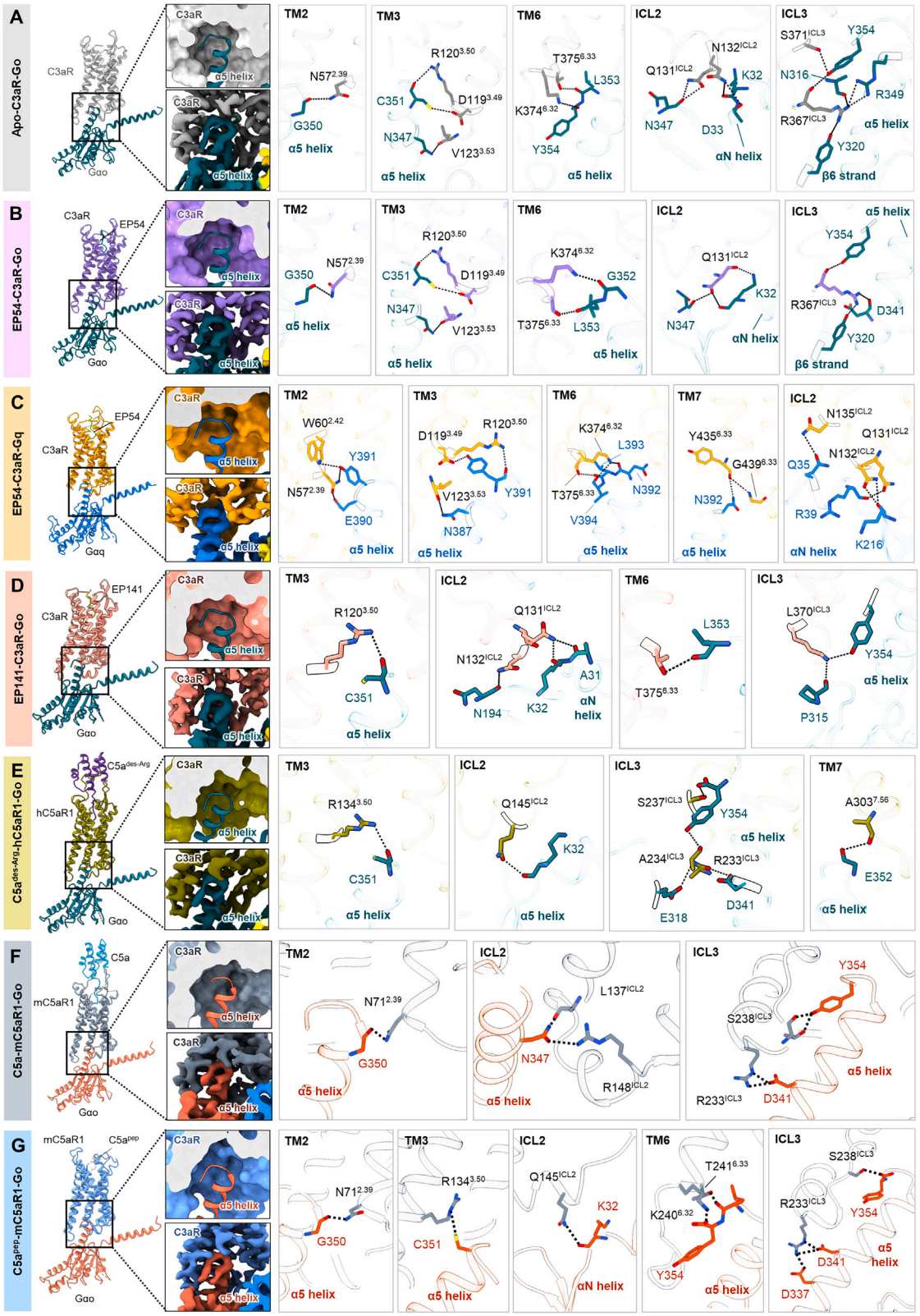

(legend on next page)

Figure S6. The G-protein interface of C3aR and C5aR1, related to Figure 6

(A–G) α5 helix of Gαo/q docks into the cytoplasmic core of C3aR and C5aR1. Only receptor and Gα are shown in ribbon representations to highlight the binding pose of G proteins with receptor core. Surface slice presentations (top) and cryo-EM maps (bottom) have been shown in inset boxes to highlight direct docking of Gα to receptors. Magnified view of the interactions between TM2, TM3, TM6, TM7, ICL2, and ICL3 of C3aR and C5aR1 with Gαo. Ionic bonds are depicted as black dashed lines.

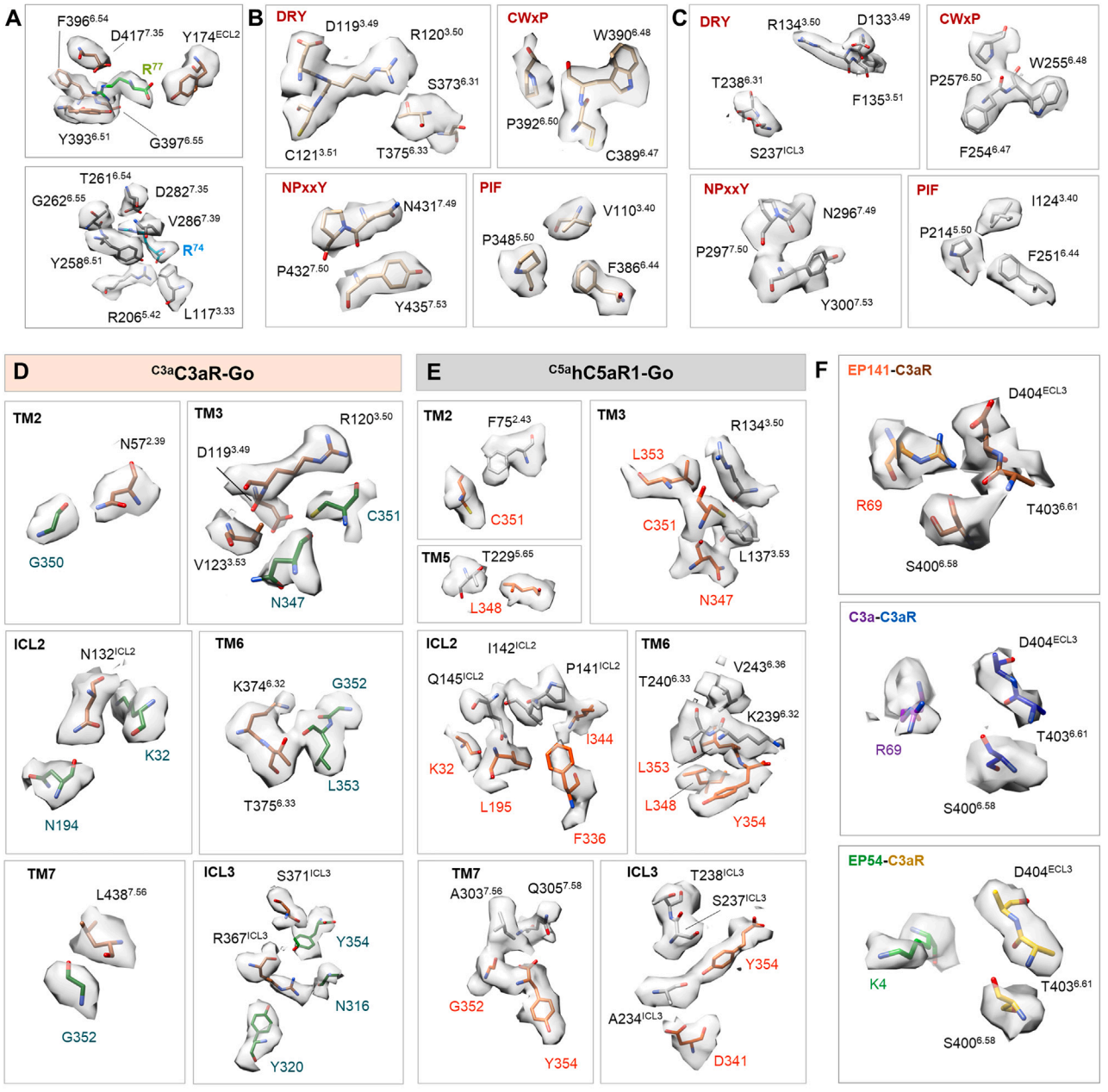

Figure S7. Cryo-EM densities of interface residues and sequence of complement peptide agonists, related to Figures 4, 6, and 7

(A–F) Densities corresponding to the amino acids shown in Figures 4B, 5C, 5D, 5F, 5H, and 7E are presented.

(G) Multiple sequence alignment of complement peptide agonists.